# Synthsis, Characterization and Application of Polypyrrole/Zeolite Composites

**Kai Yu**

Laboratory of Analytical Chemistry
*Johan Gadolin* Process Chemistry Centre
Department of Chemical Engineering
Åbo Akademi University

Åbo/Turku, Finland, 2017

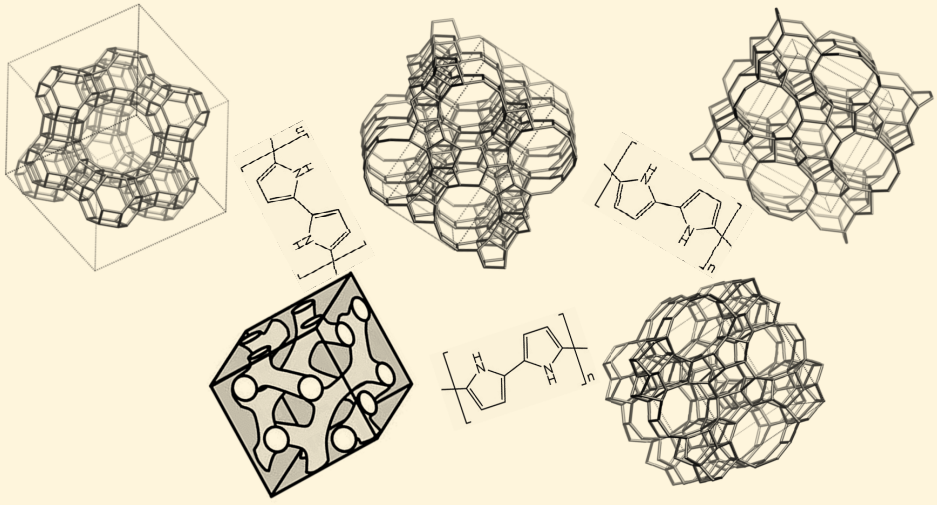

# Kai Yu

B. Sc. 2004 in Pulp and Paper Chemistry
QiLu Institute of Technology, JiNan, China

M. Sc. 2010 in Analytical Chemistry
Åbo Akademi University, Åbo, Finland

# Synthesis, Characterization and Application of Polypyrrole/Zeolite Composites

**Kai Yu**


**Laboratory of Analytical Chemistry**
**Johan Gadolin Process Chemistry Centre**
**Faculty of Science and Engineering**
**Åbo Akademi University**

**Åbo/Turku, Finland, 2017**

***Supervised by***

Professor Ari Ivaska
Laboratory of Analytical Chemistry
Johan Gadolin Process Chemistry Centre
Åbo Akademi University
Åbo/Turku, Finland

Docent Narendra Kumar
Laboratory of Industrial Chemistry and Reaction Engineering
Johan Gadolin Process Chemistry Centre
Åbo Akademi University
Åbo/Turku, Finland

***and***

Professor Johan Bobacka
Laboratory of Analytical Chemistry
Johan Gadolin Process Chemistry Centre
Åbo Akademi University
Åbo/Turku, Finland

***Reviewed by***

Professor Alain Walcarius
Laboratory of Physical Chemistry and Microbiology for the Environment
Université De Lorraine
Villers-les-Nancy, France

***and***

Professor Niklas Hedin
Department of Materials and Environmental Chemistry
Stockholm University
Stockholm, Sweden

***Dissertation Opponent***

Professor Alain Walcarius
Laboratory of Physical Chemistry and Microbiology for the Environment
Université De Lorraine
Villers-les-Nancy, France

ISBN 978-952-12-3538-2 (printed edition)
ISBN 978-952-12-3539-9 (digital edition)
Painosalama Oy – Turku, Finland 2017

## Preface

The work presented in this thesis was carried out in the Laboratory of Analytical Chemistry, Åbo Akademi University, Finland during the year of 2011-2016. Åbo Akademi Foundation, *Johan Gadolin* Process Chemistry Center, Magnus Ehrnrooth Foundation and the Rector of Åbo Akademi University are gratefully acknowledged for the financial support in my research work.

I want to express my greatest appreciation to my supervisors Professor Ari Ivaska for taking me in the laboratory and guiding my research work, and Docent Narendra Kumar for teaching me so much about the zeolites. I thank Professor Johan Bobacka for revising my thesis and answering my questions clearly and patiently. Also I would like to thank all the co-authors for their contributions in my scientific articles.

I would like to thank all my former and present colleagues at the Laboratory of Analytical Chemistry for the friendly working atmosphere. Thank you Docent Tom Lindfors, Dr. Michael Wagner, Zekra Mousavi, Ulriika Vanamo, Zhanna Boeva, Marceline Akieh and Rose-Marie Latonen for your help, discussions and suggestions in my research work. Thank you Paul Ek, Sten Lindholm and Lassi Väinölä for the equipment and technique support. A Special thanks to my Chinese friends in the Laboratory of Analytical Chemistry M.Sc. TingTing Han, Ning He, for your appreciated support in both scientific research and daily life.

衷心感谢伴我在芬兰学习和生活的中国朋友们，师兄端木，春林，徐谦，宋涛，炳之和念兴，师姐张迪，萍萍，少霞，小菊，李娜和吴昊，同届的谭琛，师弟浩林，景鑫，秦影和文洋以及师妹张雪，还有阎德，何涛。感谢你们的帮助，这个大家庭很温暖！

感谢我的妻子李玲，有了你的爱，我的生活不再孤单！谢谢你对我的理解，包容，鼓励和支持。谢谢你带给了我人生中最宝贵的礼物-嘉嘉和瑶瑶。感谢我的父亲和母亲，谢谢你们让我无忧无虑，自由自在的生活。

Åbo, April 2017

Kai Yu (于凯)

## Abstract

Hybrid materials consisting of microporous aluminosilicate zeolites and the conducting polymer polypyrrole (PPy) were synthesized and characterized. The PPy/zeolite composites exhibit both the mechanical and chemical properties of the zeolites as well as the unique electrical and electrochemical properties of PPy, which are intended for new types of catalysts and sensors.

The acid groups in the zeolites were expected to influence the properties of the PPy/zeolite composites. Therefore, the acidity of the selected zeolites was determined prior to synthesis of the composites. Because the synthetic reaction takes place in the aqueous phase, potentiometric acid-base titration was used here instead of the common gas-phase techniques. Analysis of the titration data was based on the Gran method. Various acid groups were found in the studied zeolites. Both the protonation constants and the concentrations of these acid groups were determined. The results also show that the potentiometric titration is a reliable and suitable method for characterizing the acidic properties of zeolites that are used in aqueous-phase catalytic reactions.

PPy/zeolite composites were first synthesized by chemical polymerization of pyrrole in presence of zeolites using $FeCl_3$ as the oxidizing agent. The protonated form of Beta zeolites with various $SiO_2/Al_2O_3$ ratios were used as the host for PPy in this study. Both the anionic groups in the zeolite structures and the chloride ions from the $FeCl_3$ oxidant functioned as the counter ion during the polymerization. Deposition of PPy inside the channels of the zeolite decreased the surface area of the zeolite. Some PPy/zeolite composites showed higher conductivity, compared with PPy($Cl^-$), which may be due to an increased alignment of the polymer chains in the PPy/zeolite composites.

Electropolymerization of pyrrole in presence of zeolites was performed by using the method of constant potential, resulting in electrodeposition of PPy/zeolite composites on the electrode surface. The protonated forms of Beta zeolites and Y zeolites were used in this study. The results indicate that electropolymerization of pyrrole took place mainly on the outer surfaces of the zeolite crystals. PPy was observed on the crystal surface and also in the channels of the zeolites.

The oxidized cationic PPy was charge-balanced by the anionic groups in the zeolite framework, and therefore the zeolite influenced the electrochemical behavior of PPy.

The electrodeposited PPy/zeolite composites were tested as solid contact in an ion-selective electrode (ISE). For this purpose, the protonated forms of ZSM-5 zeolites were used as the host for PPy. The anionic groups in these zeolites functioned as the counter ions for PPy during the polymerization. The results indicated that microporous zeolites containing a high concentration of anionic groups are proper candidates to form composites with conducting polymers in order to generate a new type of solid contact for ion-selective electrodes.

## Referat (abstract in Swedish)

Hybridmaterial bestående av mikroporösa aluminiumsilikat-zeoliter och den elektriskt ledande polymeren polypyrrol (PPy) framställdes och karakteriserades. PPy/zeolit-kompositerna uppvisar såväl zeoliternas mekaniska och kemiska egenskaper som de unika elektriska och elektrokemiska egenskaperna hos PPy, vilka är avsedda för nya typer av katalysatorer och sensorer.

Zeoliternas syragrupper förväntades påverka egenskaperna hos PPy/zeolit-kompositerna. Därför bestämdes surheten hos de valda zeoliterna innan kompositerna tillverkades. Eftersom syntesreaktionen äger rum i vattenfas, användes potentiometrisk syra-bastitrering i stället för de allmänna gasfas-teknikerna. Analys av titrerdata baserades på Gran-metoden. Ett flertal syragrupper hittades i de studerade zeoliterna. Både syrakonstanterna och koncentrationerna av dessa syragrupper bestämdes. Resultaten visar också att potentiometrisk titrering är en pålitlig ock lämplig metod för karakterisering av syraegenskaperna hos zeoliter som används i katalytiska reaktioner som sker i vattenfas.

PPy/zeolit-kompositer framställdes först genom kemisk polymerisering av pyrrol i närvaro av zeoliter genom att använda $FeCl_3$ som oxidationsmedel. Den protoniserade formen av Beta-zeoliter med ett antal olika $SiO_2/Al_2O_3$ förhållanden användes som värd för PPy i denna studie. Både zeoliternas anjoniska grupper och kloridjoner från oxidationsmedlet $FeCl_3$ fungerade som motjoner vid polymeriseringen. Bildning av PPy inne i zeolitens kanaler minskade zeolitens

ytarea. Vissa PPy/zeolit-kompositer uppvisade högre konduktivitet, jämfört med PPy($Cl^-$), vilket tyder på att polymerkedjorna var mera välordnade i PPy/zeolit-kompositerna.

Elektropolymerisering av pyrrol i närvaro av zeoliter utfördes med konstant-potentialmetoden, vilket resulterade i elektrokemisk beläggning av PPy/zeolit-kompositer på elektrodytan. De protoniserade formerna av Beta-zeoliter och Y-zeoliter användes för de elektrokemiskt framställda PPy/zeolit-kompositerna som studerades i detta arbete. Resultaten tyder på att elektropolymeriseringen av pyrrol företrädesvis skedde på ytan av zeolitkristallerna. PPy observerades på kristallytan och även i zeoliternas kanaler. Laddningen hos oxiderad katjonisk PPy balanserades av anjoniska grupper i zeolitens struktur, och därför påverkade zeoliten de elektrokemiska egenskaperna hos PPy.

De elektrokemiskt framställda PPy/zeolit-kompositerna testades som fast kontakt i en jonselektiv elektrod (ISE). För detta ändamål användes de protoniserade formerna av ZSM-5-zeoliter som värd för PPy. De anjoniska grupperna i dessa zeoliter fungerade som motjoner för PPy under polymeriseringen. Resultaten tyder på att mikroporösa zeoliter med en hög koncentration av anjoniska grupper är lämpliga kandidater för att bilda kompositer med elektriskt ledande polymerer som kan ge upphov till en ny typ av fast kontakt för jonselektiva elektroder.

# Table of content

## List of publications

This thesis is based on the following papers:

I. **Determination of acid sites in porous aluminosilicate solid catalysts for aqueous phase reactions using potentiometric titration method**
*Kai Yu, Narendra Kumar, Atte Aho, Jorma Roine, Ivo Heinmaa, Dmitry Yu Murzin, Ari Ivaska, Journal of Catalysis 335 (2016) 117-124*

II. **Synthesis and characterization of polypyrrole/H-Beta zeolite nanocomposites**
*Kai Yu, Narendra Kumar, Jorma Roine, Markus Pesonen, Ari Ivaska, RSC Advances 4 (2014) 33120-33126*

III. **Electrodeposition of composites consisting of polypyrrole and microporous zeolites**
*Kai Yu, Narendra Kumar, JingJing Li, Jorma Roine, Ari Ivaska, Journal of Solid State Electrochemistry 19 (2015) 59-70*

IV. **Electrosynthesized polypyrrole/zeolite composites as solid contact in potassium ion-selective electrode**
*Kai Yu, Ning He, Narendra Kumar, NianXing Wang, Johan Bobacka, Ari Ivaska, Electrochimica Acta 228 (2017) 66-75*

### Contribution of the author

The author designed the research plan with the co-authors, did most of the experimental work, and was principally responsible for writing the manuscripts.

### Supporting publications

**Synthesis and characterization of electroactive films based on benzo(a)pyrene**

*Michal Wagner, Kai Yu, Carita Kvarnström, Ari Ivaska, Electrochimica Acta 56 (2011) 3443-3446*

## Abbreviations and symbols

| | |
|---|---|
| ATR | attenuated total reflection |
| CP | conducting polymer |
| CV | cyclic voltammetry |
| $E_g$ | band gap energy |
| $E$ | potential |
| EIS | electrochemical impedance spectroscopy |
| FTIR | fourier transform infrared (spectroscopy) |
| $f(V)$ | Gran function |
| $I$ | current |
| ICP-OES | inductively coupled plasma-optical emission spectroscopy |
| IR | infrared (spectroscopy) |
| ISE | ion-selective electrode |
| ISM | ion-selective membrane |
| ITO | indium tin oxide |
| $K_{HR}^{H,R}$ | protonation constant of acid group |
| NMR | nuclear magnetic resonance |
| $pK_a$ | negative logarithm of acid group protonation constant |
| PPy | polypyrrole |
| $R^-H^+$ | acid group in zeolite |
| SEM | scanning electron microscopy |
| TEM | transmission electron microscopy |
| TPD | temperature-programmed desorption |
| $V$ | volume of added base |
| $V_0$ | initial volume of the sample solution |
| $V_{eq}$ | equivalence volume |
| XRD | X-ray powder diffraction |
| $Z'$ | real component of impedance |
| $-Z''$ | imaginary component of impedance |

# 1. INTRODUCTION

Combination of conducting polymers with organic/inorganic materials has been intensively studied for producing new types of hybrid materials. The organic materials can be polymers [1] or biologically active species [2]. The inorganic materials can be metals such as Ag, Au and Ti and their oxides [3-5], carbon-based materials including carbon nanotubes, graphene and graphene oxide [6, 7], and cellulose [8]. The synthesis methods are polymerization, dispersion, redox reaction, and electrostatic interaction [9]. Since the chemical and physical properties of the conducting polymer as well as the incorporated materials will be modified, the resulting composites may exhibit enhanced optical, electronic, chemical and mechanical properties as well as environmental stability. Hence, these composites are promising for applications in e.g. supercapacitors and chemical/biological sensing devices.

Zeolites, an inorganic microporous/mesoporous solid, have gained the attention from electrochemical community in the past decades [10]. These aluminosilicates based materials consist of well-defined uniform cages and channels, and also have high degree of open porosity, physical and chemical stability as well as acidic property [11, 12], which make them of high interest in the design of new inorganic/organic composites. To date, functioning as the 'modifier' in a chemically modified electrode is the most commonly application of zeolites in the electroanalytical field. Such electrodes are also known as the zeolite modified electrodes, and the sensing material is general composed by zeolites and conducting polymers or zeolites and conducting matrix (e.g. carbon particles). The features of zeolites mentioned above are expected to favor the mass transport and/or the charge transfer at the electrode, and meanwhile improve its selectivity and long-term durability [13].

In this thesis work, the protonated forms of microporous zeolites were used as the inorganic matrix for the conducting polymer polypyrrole (PPy). Both chemical and electrochemical methods were applied for synthesizing the PPy/zeolite composites. Fundamental studies of PPy/zeolite composites can help us to choose the proper zeolite when synthesizing this type of material. In addition, the potentiometric acid-base titration instead of the traditional gas-phase methods was tested for characterizing the anionic groups in the zeolites.

# 2. ZEOLITES

## 2.1. Zeolites in general

Zeolites are crystalline aluminosilicates with a three-dimensional framework of porous structure. The word 'zeolite' stems from two Greek words 'zeo' and 'lithos', which mean boil and stone. This material occurs in nature and has been known for 250 years [14]. Today, there are about 40 types of natural zeolites, which are mainly found in volcanic and sedimentary rocks, and nearly 200 types of synthetic zeolites have been designed and fabricated for specific purposes. Zeolites are widely used in daily life and in industrial applications, e.g. as water softeners, animal food, adsorbents, and in industrial catalysis reactions, especially in the field of petroleum refining and synthesis of petrochemicals [15, 16]. In recent years, acidic and metal (include transition and noble) modified zeolite catalysts have found applications for synthesis of pharmaceuticals, specialty and fine chemicals [17].

The general chemical composition of both natural and synthetic zeolites can be represented by the following formula:

$$C_{y/n}^{n+}[(SiO_2)_x \cdot (AlO_2)_y] \cdot zH_2O$$

where ($x$+$y$) is the number of tetrahedral per crystallographic unit cell, $x/y$ is the molar ratio between silicon and aluminum in the zeolite framework, $z$ is the amount of water which may be reversibly removed by heat, and C is a cation with the charge $n$, such as $Na^+$, $K^+$, $NH_4^+$, $Mg^{2+}$ and $Cu^{2+}$. Because the cation can readily be exchanged with other cations, zeolites are highly effective as ion exchanger and adsorbent.

Meier and Olson classified the zeolitic materials based on their framework types in 1970, and the classification was then accepted by the zeolite community [18]. The rigid three-dimensional framework of zeolite consists of corner-sharing $TO_4$ (T = Si, Al) tetrahedral building units, which are coordinated with each other by shared oxygen atoms [19]. This framework is relatively open due to the presence of various porous systems including channels, channel intersections and/or cavities. Pore openings are depending on the size of the ring, which is related to the number of T-atoms/O-atoms in one ring. For example, an 8-ring is considered to be a small pore opening with the diameter of 0.41 nm, a 10-ring is a medium one (0.55 nm), and a 12-ring is a big one (0.74

nm). These rings connect with each other and form various subunits and cages. As a result, numerous types of zeolite frameworks can be produced. Some of the subunits and cages are shown in Fig. 1 [20]. As can be seen, a double 6-ring unit is composed by six 4-rings and two 6-rings, while a sodalite unit is defined by six 4-rings and eight 6-rings. The exploitable properties of the zeolites are essentially determined by their framework structures, e.g. the ion-exchange selectivity depends on the number and nature of the acid groups and their accessibility, the sorption capacity depends on the pore opening size and the void volume, and the catalytic behavior upon the dimensionality of the porous system, the acid groups, and the space available for the catalytic reaction [21-23].

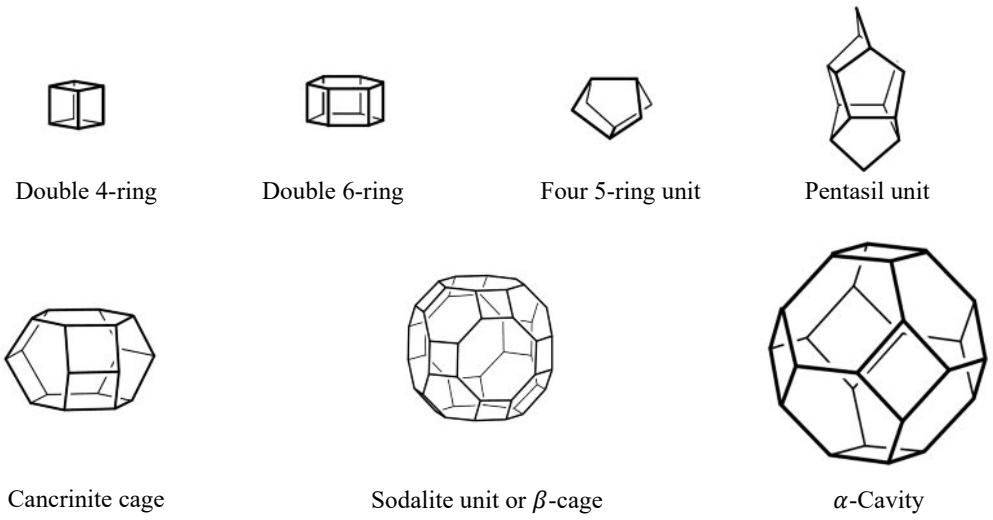


Fig. 1 Typical subunits and cages present in zeolite frameworks

The studied zeolites in this research work are Beta, Ferrierite, Y, ZSM-5 with the framework type codes of BEA, FER, FAU, MFI, and a pristine silica mesoporous material Si-MCM-48 which has no aluminum in its framework. It should be noted that the three-letter codes are not the name of the zeolites, but indicate the structure of these materials. As can be seen in Fig. 2, different

subunits and cages compose the frameworks of these zeolites, resulting in various porous systems.

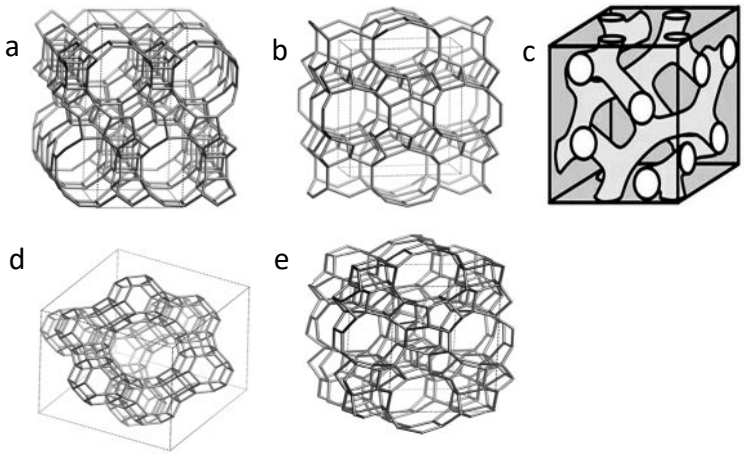


Fig. 2 Frameworks of the studied zeolites, a) BEA, b) FER, c) Si-MCM-48, d) FAU and e) MFI

The structural features of these zeolites are listed in Table 1. The three-dimensional structure of the Beta zeolite has two channel systems: one channel consists of 12-membered rings with dimensions of 5.6 × 5.6 Å and the other consists of 12-membered rings with dimensions of 6.6 × 6.7 Å. The two-dimensional structure of the Ferrierite zeolite contains two types of channels as well: one channel composed by 8-membered rings with dimensions of 3.5 × 4.8 Å and the other composed by 10-membered rings with dimensions of 4.2 × 5.4 Å. The three-dimensional cubic structure of Si-MCM-48 consists of unconnected pore systems with dimensions of 20-80 Å [24-26]. The three-dimensional pore system of Y zeolite contains one tetragonal crystal system: supercage, which shares a 12-membered ring with dimensions of 7.4 × 7.4 Å [27]. The ZSM-5 zeolite has a three-dimensional network consisting of straight and sinusoidal 10-ring channels with pore diameters of 5.1 × 5.5 and 5.3 × 5.6 Å, and also has an intersection with dimension 9 Å [28].

Table 1 Structural feature of the studied zeolites, and Si-MCM-48 mesoporous material

| Zeolites | Framework type code | Ring | Pore aperture size (Å)* | Dimensionality of pore system | Connectivity between different pore system |
|---|---|---|---|---|---|
| Beta | BEA | 12 | $5.6 \times 5.6^{I}$ | 3 | Interconnected |
| | | 12 | $6.6 \times 7.7^{II}$ | | |
| Ferrierite | FER | 8 | $3.5 \times 4.8^{I}$ | 2 | Interconnected |
| | | 10 | $4.2 \times 5.4^{I}$ | | |
| Si-MCM-48 | | | 20 – 80 | 3 | |
| Y | FAU | 12 | $7.4 \times 7.4^{III}$ | 3 | |
| ZSM-5 | MFI | 10 | $5.1 \times 5.5^{I}$ | 3 | Interconnected |
| | | 10 | $5.3 \times 5.6^{I}$ | | |

*The superscript indicates that the channel is (I) one-, (II) two-, or (III) three-dimensional.

### 2.2. Acidic property of zeolites

As described above, the basic structural unit of zeolite framework is the $SiO_4$ or $AlO_4$ tetrahedra with O atoms connecting neighboring tetrahedral [29]. A heteroatom such as Al, B, Ga and Fe, which has a lower valency than Si, is introduced to the framework and the formal charge on that tetrahedron changes from neutral to negative. This negative charge is then balanced either with a proton to form a strong Brønsted acid group or with a metal cation to form a weak Lewis acid group [30], as shown in Fig. 3.

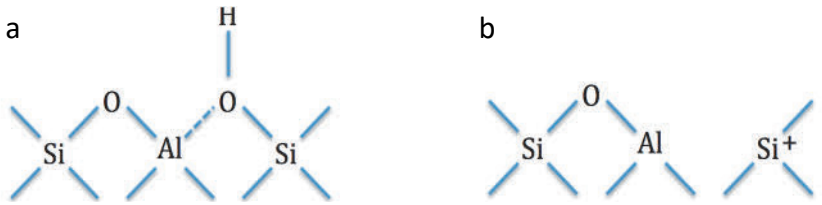


Fig. 3 Schematic representation of the acid groups in zeolites, a) Brønsted acid group and b) Lewis acid group

Due to the presence of the acid groups in the framework, the solid acid and metal modified zeolites are used as catalytic materials in several petro-chemical and oil refining processes, as well as in synthesis of fine and specialty chemicals [31, 32]. Acidic and metal modified zeolite

catalysts are also used in environmental applications such as exhaust gas purification from mobile and stationary sources, pretreatment of industrial and municipal wastewater streams, agricultural soil contamination and nuclear waste treatment [33-36]. Since these acid groups play an important role in the catalytic and sorption properties of zeolites [37], better knowledge of them is important for successful industrial applications of zeolites as solid catalysts.

### 2.2.1. Formation of acid groups in zeolites

Brønsted acid groups dominate the catalytic properties of zeolites, thus the activity of zeolites is based on the concentration and the type of Brønsted acid groups in their frameworks. Three methods are mainly applied to generate the Brønsted acid groups/acidic OH groups in the synthetic zeolites. The most common method is to replace the alkali metal cations or alkylammonium cations in the zeolite framework with the protons to obtain the OH groups. For example, in this thesis the Beta zeolite that is initially in its Na-form is first converted into its ammonium form ($NH_4$-Beta) by ion-exchange with ammonium nitrate. $NH_4$-Beta is then converted into the protonated form (H-Beta) by decomposing $NH_4^+$ ions at 450 ℃ for 4 hours. The transformation can be expressed as follows (Fig. 4):

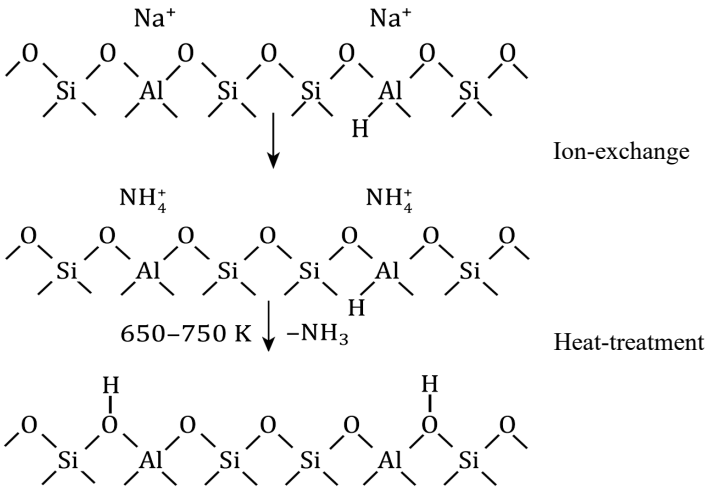


Fig. 4 Formation of acidic OH groups for zeolites by replacing the alkali metal ion with proton

The second way is by ion-exchange with multivalent cations, i.e. $Ca^{2+}$, $Mg^{2+}$, and $La^{3+}$. As shown in Fig. 5, the introduced multivalent cations are coordinated with water molecules and are in the zeolite framework in the form of $[Ca(H_2O)]^{2+}$, $[Mg(H_2O)]^{2+}$, and $[La(H_2O)]^{3+}$. With heat treatment, the water molecule will be dissociated, thereby generating the acidic OH groups for the zeolite [38, 39]. It has been found that the amount of Brønsted acid group increases with decreasing size of multivalent cations: Ba/zeolite < Sr/zeolite < Ca/zeolite < Mg/zeolite.

$$[Ca(H_2O)]^{2+} \rightarrow [Ca(OH)]^{+} + H^{+}$$

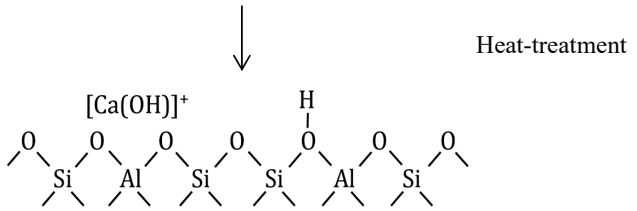


Fig. 5 Formation of acidic OH groups in zeolites by ion-exchange with multivalent cations

In the third method, the acidic groups are formed by reduction of transition metal cations such as $Cu^{2+}$ and $Ag^{+}$. These cations are introduced to the zeolite framework via ion-exchange and then reduced by gaseous hydrogen. The generated protons are trapped by the framework oxygen, thus forming the acidic OH groups [40-42].

### 2.2.2. Factors affecting acid strength of acid groups

The concentration of acidic OH groups is basically determined by the Si/Al molar ratio in the zeolite framework. A high Si/Al ratio diminishes the concentration of OH groups [43, 44]. However, the acid strength of the OH groups depends on various factors. Theoretical calculations show that the acidity of bridging hydroxyl groups is greatly influenced by the zeolite structures. The angle of the Si-O-Al bond as well as the length of the Si-O and Al-O bonds will be changed when the proton is removed from the bridging hydroxyl groups, indicating that the deprotonation

energy is determined by the local structure of the zeolite. Carson et al. noted that increase in the Si-O-Al angle can decrease the deprotonation energy of the bridging hydroxyl groups, and thus enhance the acidic strength of the OH groups [45]. Katada et al. found that a shorter distance of the Al-O bond gives a stronger interaction between Al and the OH, resulting in a smaller charge and a higher acid strength of the OH group. This has been confirmed by the acid strength order MFI > BEA > FAU [46]. The acidic properties of zeolites can be changed by isomorphous substitution of Al in the framework with Be, B, Ti, Cr, Fe, Zn, Ge, Ga and V. These elements are introduced to replace the aluminum by adding the metal salts in the starting gel solution when synthesizing the zeolites. Both the acidic and the redox properties of the zeolites are thus modified with the new elements. For example, Chu et al found that the acid strength of the OH groups in various metallosilicates with MFI structure decreases as follows [47]:

[Al]-ZSM-5 > [Ga]-ZSM-5 > [Fe]-ZSM-5 > [B]-ZSM-5

### 2.2.3. Traditional acidity characterization methods for zeolites

Numerous gas phase methods and techniques have been published to quantify and characterize the acidity of zeolites. One of the methods uses Fourier Transform Infrared (FTIR) spectroscopy of various probe molecules (ammonia, pyridine) adsorption to study the fundamental stretching vibrations of hydroxyl groups at varying temperatures to determine the Brønsted and Lewis acid groups [48, 49]. Another commonly used method is the temperature-programmed desorption (TPD) technique to measure the reacted amount of a gaseous base (ammonia) with zeolites for characterizing the density and strength of the acid groups [50]. Both FTIR-pyridine and TPD-ammonia methods are performed in the gas phase at high temperature (100 – 450 ℃). However, many catalytic reactions, especially those related to valorization of biomass, are carried out in aqueous solutions at room or somewhat elevated temperature [51, 52]. Therefore, the catalytic properties based on the acidity of the zeolites determined with FTIR-pyridine and TPD may not be relevant. Additionally, the goal of this research work is that the acid groups on the zeolites' framework will function as the counter ions for PPy when synthesizing the PPy/zeolite

composites in water solution. A technique which can be used to characterize the acidic properties of the zeolites in the aqueous phase is therefore necessary.

Acid-base titration of zeolites in non-aqueous solvents has been used earlier to study the acidity of zeolites. The method was introduced by Benesi in the 1950s [53] and then modified by other researchers [54]. In that method, the surface of zeolite was titrated with amine, i.e. *n*-butylamine, in a non-aqueous solvent. A series of Hammett indicators with various acidity constant values, i.e. benzeneazodiphenylamine ($pK_a$ = 1.5) and phenylazonaphthylamine ($pK_a$ = 3.3), were used to characterize the acid groups [55]. However, it was demonstrated later that the additional indicators in the non-aqueous solvent could disturb the equilibrium state of the zeolite system during the titration [56, 57]. Another drawback of using the Hammett indicators is their molecular size, which is too large for the indicator molecules to enter the channels and cages of some zeolites [58]. Due to these fundamental limitations and the long time of the experiments, the titration using indicators did not become a popular technique in characterizing the acid groups of zeolites.

### 2.2.4. Potentiometric acid-base titration method

In this research, a specific potentiometric acid-base titration method developed from the traditional titration method was tested to characterize the acidity of zeolites. This method has a high resolution in determining the various acid groups present in the samples. Moreover, it is not necessary to use any indicators to monitor the acid-base reaction. During the titration, pH of the solution is measured as a function of the volume of a strong base added and the obtained titration curve is used to analyze the samples. In addition, the small $OH^-$ ions can penetrate deep inside the zeolite channels and the acid groups in those channels can therefore also be determined.

The acid-base properties of zeolites in aqueous solutions can best be described by considering that the material contains several different acid groups with different strengths, i.e. different protonation constants, according to the following equilibria and constants:

$$R_1^- H^+ \rightleftharpoons R_1^- + H^+; K_1 = \frac{[R_1^- H^+]}{[R_1^-][H^+]}$$

$$R_2^- H^+ \rightleftharpoons R_2^- + H^+; K_2 = \frac{[R_2^- H^+]}{[R_2^-][H^+]}$$

……

……

$$R_n^- H^+ \rightleftharpoons R_n^- + H^+;\ K_n = \frac{[R_n^- H^+]}{[R_n^-][H^+]}$$

where $R$ denotes the anionic part of the acid group, $K_n$ is the protonation constant of the acid group. It should be pointed out that the concentrations of the different $R$ ($R_1$, $R_2$, ..., $R_n$), i.e. acid groups, are also different.

The Gran method, which is based on Sørensen's [59] earlier work and described by Gran in 1950 [60], was selected for the titration data analysis in this work (Table 2). The common sigmoidal potentiometric titration curve is transformed to a linear form with the Gran functions, which allows calculation of the equivalence volume ($V_{eq}$) by a standard linear regression method using several points on the titration curve. The Gran functions used in this work and their derivations are shown in the supplementary information (S). Ingman and Still have derived a more accurate equation than (S14) in the supplement to describe the titration of a weak acid with strong base [61]. Ivaska and Wänninen have developed that method further for simultaneous determination of both $V_{eq}$ and $K$ by an iterative computing method [62]. The Gran function can be used when the electrode system has a Nernstian response and the activity coefficients of the species in the solution remain constant during the potentiometric titration.

Table 2 Gran functions (from the Supplement) used for analysis of the potentiometric titration data. $V_0$ is the initial volume of the sample solution, $V$ is the volume of titrant added, $C_{OH}$ is the concentration of the titrant and $K$ is the protonation constant of the acid (***Table 1, Paper I***)

| | **Gran Functions** | |
|---|---|---|
| **Substance titrated** | **On the acid side of the equivalence point** | **On the alkaline side of the equivalence point** |
| Strong acid | $f_1(V) = \frac{(V_0 + V)}{C_{OH}} \cdot 10^{-pH}$ | $f_2(V) = \frac{(V_0 + V)}{C_{OH}} \cdot 10^{(pH-14)}$ |
| Weak acid | $f_3(V) = K \cdot 10^{-pH} \cdot V$ | $f_2(V) = \frac{(V_0 + V)}{C_{OH}} \cdot 10^{(pH-14)}$ |

A conventional titration curve, i.e. pH as function of $V$ (volume of added base), for titration of the strong acid $HNO_3$ with the strong base NaOH is shown in Fig. 6. When the same experimental data (pH vs. $V$) are processed with the Gran functions $f_1(V)$ and $f_2(V)$, the two straight lines in Fig. 6 are obtained. The numerical scales for $f_1(V)$ and $f_2(V)$ are different and not shown in the figure. The lines intersect each other on the $V$-axis at $V_{eq}$, which is known as the equivalence volume of the titration and can be used in calculating the concentration of $HNO_3$. Both lines can be used in determination of $V_{eq}$.

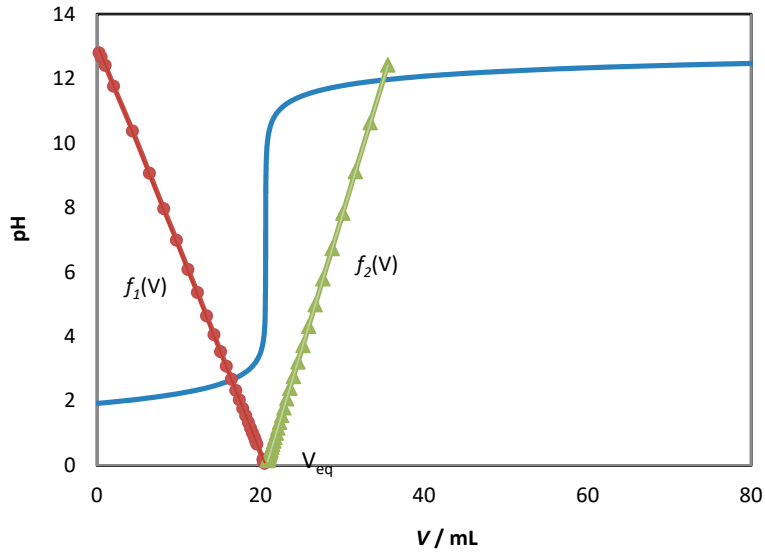


**Fig. 6** Titration of 4 mL of 0.5 M $HNO_3$ with 0.1 M NaOH. The ▬ line is pH vs. $V$ (volume of added base). The linear Gran curves obtained with $f_1(V)$ and $f_2(V)$ have the same intersection point on the $V$-axis and the point is the equivalence volume ($V_{eq}$). The ● and ▲ on curves $f_1(V)$ and $f_2(V)$ show the positioning of the data points used for evaluating the $V_{eq}$ (***Fig. 2, Paper I***)

The computer program FITEQL is also used to calculate the protonation constants and the concentrations of the acid groups in the studied zeolites. This method is based on the equations of chemical equilibria [63]. The experimental data includes the concentration of the titrant, pH, dilution factor, and ionic strength of the solution, which are entered as input parameters to the program. Both the protonation constants $lgK_{HR}^{H,R}$ and the concentrations of the acid groups are first guessed for the equilibrium calculation, and the two values are then optimized by an iterative procedure on the adjustable parameters in the FITEQL program. The program is running with the following steps [64]:

1. Definition and input of the chemical equilibrium model
2. Input of free concentration, total concentrations and $K_{HR}^{H,R}$ values of known species
3. Input of the initial guesses for the concentrations and $K_{HR}^{H,R}$ values of unknown species
4. Input of the experimental titration data, i.e. $C_{OH,}$ pH, dilution factor, and the ionic strength of the solution

5. Start the calculation
6. The initial guesses are set to the equilibrium values by proceeding the iterations on the adjustable parameters in the program
7. Output of optimum values for the concentrations and the protonation constants ($lgK_{HR}^{H,R}$)

# 3. CONDUCTIING POLYMERS

A conducting polymer (CP) is an organic polymeric molecule that can possess intrinsic electrical conductivity after doping. The modern CP research is considered to start from doping of polyacetylene with bromine. Hideki Shirakawa found that the conductivity of the doped polyacetylene was 10 million times higher than the undoped state. Because of this important discovery, Shirakawa won the Nobel Prize in Chemistry together with Alan J. Heeger and Alain G. MacDiarmid in the year of 2000 [65]. The CP backbone consists of alternating single and double bonds (conjugated double bonds) that are responsible for the unusual electronic property of such material [66]. Some commonly studied CPs with their molecular structures (in their neutral, undoped state) are shown in Fig. 7. The specific bond network and also the heteroatoms, i.e. N and S, in the polymer chain give the CPs various electronic properties.

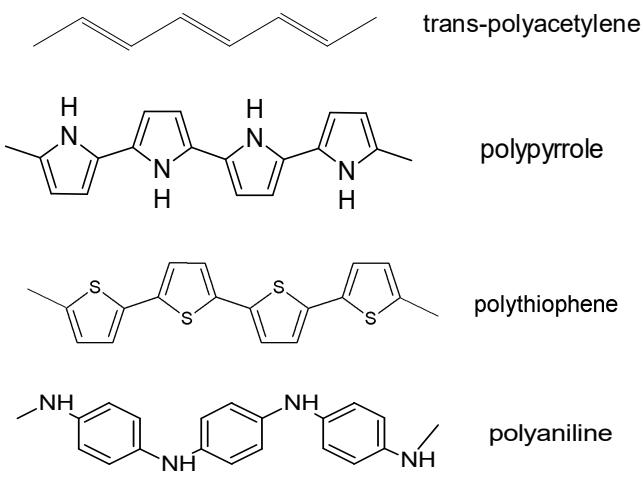


Fig. 7 Molecular structures of some conducting polymers

### 3.1. Chemical and electrochemical synthesis

CPs can be prepared either by chemical and/or by electrochemical polymerization. In chemical polymerization, the chain growth of the CP is due to the oxidation of the CP monomer by using catalysts or reagents, and the mechanism is similar to that of electrochemical polymerization. The CP is commonly obtained in an oxidized state, and the counter ions existing on the polymer chain are from the electrolyte salt used in the reaction. Chemical polymerization is recommended for producing bulk quantities of CPs [67]. However, the electrochemical polymerization is preferable if the CPs is intended to be a thin-layer film or in micro scale. The experimental setup for the electrochemical polymerization is either two electrodes (working and counter) or three electrodes (working, counter and reference), which are mounted in an electrolysis cell. CP films are deposited on the surface of the working electrode, and the commonly used materials for this electrode are gold, platinum, glassy carbon as well as transparent indium-tin oxide-coated glass [68].

Electrochemical polymerization of CPs can be performed by using the potentiodynamic method (cyclic voltammetry: continuous variation of potential), the potentiostatic method (application of a constant potential), and the galvanostatic method (application of a constant current) [69]. The potentiodynamic method is used particularly when studying the growth rate of CPs and generally results in high-quality films with good substrate adhesion [70]. In the galvanostatic method the polymerization rate is constant, but some unwanted side reactions may occur if the potential increases as the CP film grows. The potentiostatic method allows to avoid the side reactions because of the applied constant potential. Compared with the potentiodynamic way, the CPs are obtained in their doped state when synthesized by the potentiostatic or the galvanostatic method [69, 70].

The electropolymerization mechanism of a CP starts with oxidation of the CP monomers generating radical cations (see Fig. 11). Propagation via *a)* dimerization reaction in which two radical cations form a dimer; *b)* electrochemical oxidation of the dimer giving an oligomeric radical; *c)* combination of this oligomeric radical with radical cations, and repetition of steps *a* and *b* can thus build up the polymer [71, 72]. However, the chain growth may also proceed by dimers coupling with dimers to form tetramers that generate octamers and further polymers [70,

73]. The physical and electrochemical properties of the prepared CP are depending on the experimental conditions, e.g. the composition of the solution, the defined potential window or the rate of the potential change in potentiodynamic polymerization, the galvanostatic current density, the material of the electrode, the initial state of the electrode surface, and even the reaction temperature [70].

When using electrochemical polymerization, the thickness of the conducting polymer film can be controlled by varying the potential or current with time. In addition, the electrochemical method can provide an *in-situ* way to investigate the polymerization process and also the properties of the resulting conducting polymer.

### 3.2. Doping

Depending on the 'width' of the band gap or energy gap ($E_g$), materials are divided into three groups, i.e. metals, semiconductors and insulators. As shown in Fig. 8, the energy difference between the conduction band and the valence band determines the 'width' of the gap. There is no gap in a metal due to the overlapping of the two bands. Both semiconductors and insulators have a band gap between the conduction and valence bands.

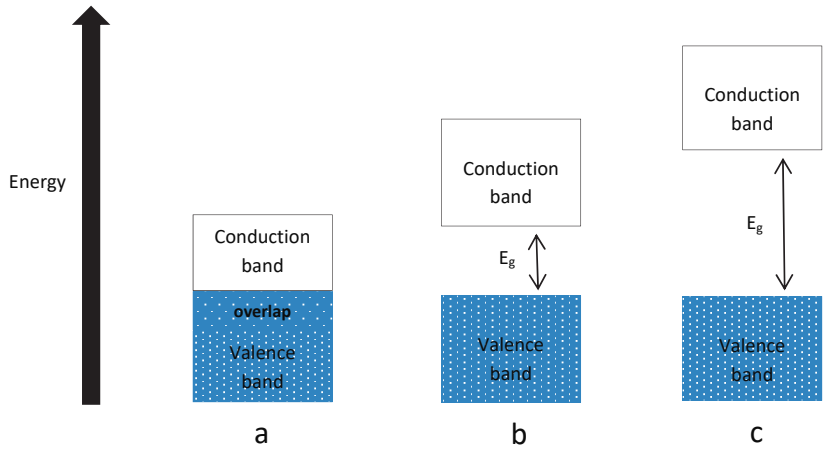


Fig. 8 Schematic presentation of band gap ($E_g$) in: a) metal, b) semiconductor and c) insulator

A neutral CP belongs to the category of semiconductors or even insulators. However, the electronic state of the CP can be changed from insulator to conductor with doping. Both chemical and electrochemical methods can be used for this purpose [74]. The chemical way includes p-doping and n-doping, and the principles can be presented schematically by the following reactions:

Chemical p-doping: $C + A \rightarrow C^{+}A^{-}$ Eq. 1

Chemical n-doping: $C + D \rightarrow C^{-}D^{+}$ Eq. 2

where *C* (electrically neutral sate of CP) is oxidized by *A* (electron acceptor) in the chemical p-doping (Eq. 1), or reduced by *D* (electron donor) in the chemical n-doping (Eq. 2).

Electrochemical doping is achieved by changing the voltage applied to the working electrode, which has the CP film on its surface. As shown in Eq. 3 and Eq. 4, electrons are either removed from (oxidation, p-doping) or added to (reduction, n-doping) the chain of CP during the doping process. Thus, the charge carrier in p-type CP is a hole while in n-type CP it is an electron. In order to maintain the electroneutrality the created charge on the polymer chain needs to be balanced by the counter ion (or dopant) [71]. The counter ion will move into the CP during the oxidation and out from the CP during the reduction [73]. The doping level refers to the number of charges per monomer unit that are created in the polymer chain [75].

Electrochemical p-doping: $C + M^{-} \rightarrow C^{+}M^{-} + e^{-}$ Eq. 3

Electrochemical n-doping: $C + e^{-} + N^{+} \rightarrow C^{-}N^{+}$ Eq. 4

where *C* (electrically neutral sate of CP) is oxidized and balanced by counter ion ($M^{-}$) in the electrochemical p-doping (Eq. 3), or reduced and balanced by counter ion ($N^{+}$) in the electrochemical n-doping (Eq. 4).

To date, the range of the conductivity of CPs is found from $10^{4}$ to $10^{-10}$ S/cm, which is determined by the polymer itself, the dopants and the doping level [76].

### 3.3. Applications of conducting polymers

The specific properties such as electrical conductivity, magnetic, optical, wettability, mechanical and microwave absorbing properties of conducting polymers can give them an extensive range of applications [77]. Fig. 9 illustrates important applications of such materials, i.e. nonvolatile memory devices, microwave absorption and EMI shielding, biomedical applications, electrorheological fluids, energy storage, catalysis, sensors, and electronic nanodevices [78].

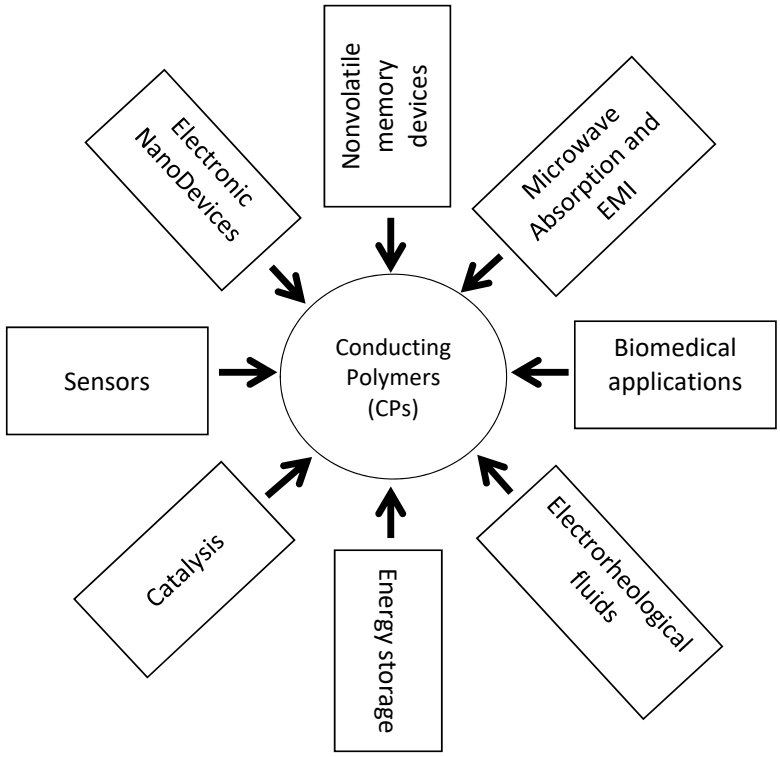


Fig. 9 Applications of conducting polymers

### 3.4. Polypyrrole

Polypyrrole (PPy) (molecular structure shown in Fig. 7) is one of the CPs that has been most intensively studied due to its inherent advantages such as tunable electrical conductivity, good environmental and thermal stability, good mechanical properties, and easy and flexible way to synthesis [79-82]. The pyrrole monomer exhibits good solubility in aqueous and non-aqueous solvents. Since pyrrole has a lower oxidation potential than water, it can be synthesized in aqueous solution (as well as in non-aqueous solutions) [83]. Importantly, the monomer size of pyrrole is small enough to enter the pores and channels of the zeolites studied in this work (Fig. 10) [84].

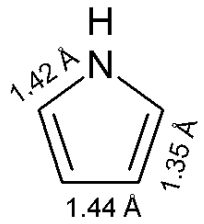


Fig. 10 Molecular size of pyrrole monomer

PPy can be prepared either by chemical or by electrochemical polymerization [85-87]. The chemical way will generate a fine powder of PPy, and using $FeCl_3$ as the oxidizing agent and water as the solvent can give PPy a high conductivity [88]. The chain growth of PPy in the electrochemical polymerization is shown Fig. 11, which is based on the E $(CE)_n$ mechanism. It starts with electron transfer (E), and is followed by chemical reaction (C) and electron transfer reaction (E) [89]. According to this mechanism, the pyrrole monomer is first oxidized on the surface of the working electrode to form a radical cation. Two radical cations are then coupled at the α-positions (the highest spin density position on the resonance structures of the radical cation) to form a dihydromer dication. A neutral aromatic dimer is obtained after the loss of two hydrogen ions from the dihydromer dication, the driving force for this step being the return to aromaticity. Compared with the monomer the dimer has a lower oxidation potential, so the polymerization is thus continued via oxidation of the dimer. Trimer formation follows the

monomer radical cation and dimer radical cation coupling and hydrogen ions releasing (deprotonation). Propagation continues by repeating the oxidation, radical coupling, and deprotonation until the final insoluble polymer (PPy) film is obtained on the electrode [90, 91].

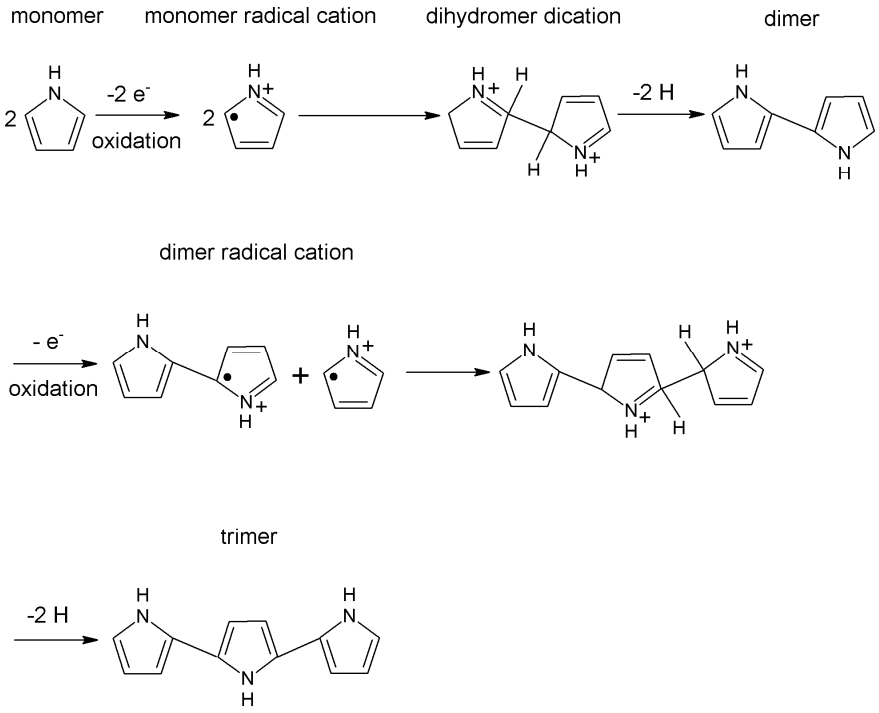


Fig. 11 Schematic representation of electrochemical polymerization of pyrrole [92]

# 4. ANALYTICAL TECHNIQUES AND METHODS

The experimental techniques and the instruments including potentiometric titration, cyclic voltammetry, Fourier transformed infrared attenuated total reflection spectroscopy used for characterizing the anionic groups in the zeolites, as well as the physical and electrochemical properties of PPy/zeolite composites, are briefly described in this chapter.

## 4. 1. Potentiometric acid-base titration

Potentiometric acid-base titration of the zeolites was carried out with an automatic titration system Mettler Toledo DL 50, Schwerzenbach, Switzerland (Fig. 12). The titrator is microprocessor controlled and the potential (pH) is measured with a combined pH glass-reference electrode with a ground sleeve junction (DG111-SC, Mettler Toledo).

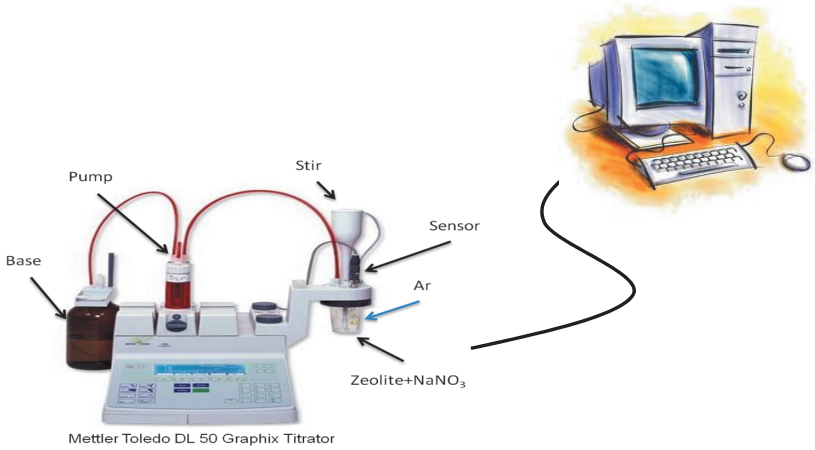


Fig. 12 Automatic potentiometric acid-base titration system

Standard sodium hydroxide (NaOH) solution was prepared as the titrant and stored in a sealed bottle under argon environment. Special care is taken to prevent contamination by atmospheric

carbon dioxide. During the titration, the titrant will be first pumped from the bottle to a burette, and then pushed into the sample suspension. A defined program records the potential change within a preset time, including a given waiting time up to the next NaOH addition. Also, the volume of the added titrant within a defined potential difference is controlled during the whole titration procedure. Both the equilibrium potential and the volume of consumed titrant are recorded at the same time, which were then used to calculate the concentrations of the anionic groups in the zeolite sample. The potentiometric pH electrode was calibrated by using standard buffer solutions of pH 4.00, 7.00 and 10.00 prior to the measurement, and the ionic strength of the titrant as well as the sample suspension were maintained at the same level by having the same concentration of sodium nitrate ($NaNO_3$).

In ***Paper I, II, III*** and ***IV*** potentiometric acid-base titration was used to characterize the acidity of the studied zeolites.

### 4. 2. Cyclic voltammetry

Cyclic voltammetry (CV) has been extensively used to synthesize CPs and study their redox behaviors. This method is generally performed in a three-electrode electrochemical cell where the potential is cycled between two values (from $E_1$ to $E_2$) at a certain scan rate. The scan is reversed when the potential reached $E_2$, and then cycled back to $E_1$. The potential is measured between the working electrode and reference electrode, whereas the current caused by the redox reaction is recorded between the working electrode and the counter electrode. This procedure can be repeated continuously. Plotting of the current ($I$) versus the applied potential ($E$) results in a cyclic voltammogram [93]. An example of a cyclic voltammogram of PPy/H-Beta-25 composite film recorded in 0.1 M NaCl solution is shown in Fig. 13. Both oxidation and reduction peaks exist on this cyclic voltammogram indicating the redox property of this material. The shape of the voltammogram depends on the electrolyte salt and solvent, potential scan rate, and film thickness etc. [67, 94]. Beside the redox behavior, other information can also be obtained from the CV, i.e. the rate of the film growth, charging capacity, charge transfer, and charge transport processes and mechanism [95].

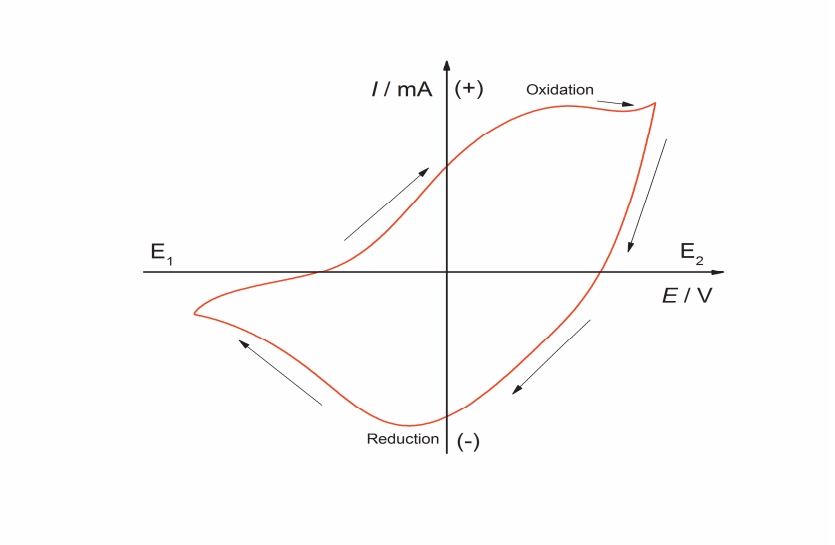


Fig. 13 Cyclic voltammogram of PPy/H-Beta-25 composite film recorded in 0.1 M NaCl solution (***Fig. 3a, Paper III***)

### 4. 3. Fourier transformed infrared attenuated total reflection spectroscopy

Infrared radiation (IR) can be absorbed when it passes through a sample while the transition between quantized vibrational states of the molecules in this material is measured. IR absorption occurs only when the vibration mode of the molecule is associated with a change in the permanent dipole moment. Each material is a unique combination of atoms and therefore results in a unique IR spectrum. During Fourier transformed infrared spectroscopy (FTIR) measurement the signal from a sample is decomposed into its component wavelengths with an interferometer and the spectrum of this sample can be obtained with the calculation of these interferograms by Fourier analysis [96]. The spectrum is a plot of absorption intensity vs. wavenumber and the peaks of the spectrum are due to the vibrations of molecular excitations [97, 98].

There are three operation modes of FTIR: transmission, reflection and attenuated total reflection (ATR) [99]. Since FTIR by attenuated total reflection is available for all types of samples (e.g. solids, liquids, powders and fibers), it has been selected to characterize the molecular structures of the pristine zeolites and the PPy/zeolite composites in this thesis. Compared with the

transmission and reflection spectroscopy, the infrared radiation is not transmitted through the sample in ATR measurement. Therefore, the thickness of the sample does not have to be thin enough to allow the transmission of the infrared beam when using the ATR technique.

The basic principle of ATR measurement is shown in Fig. 14. The sample to be studied is placed on the ATR crystal, which is also known as the sensing element. The materials of the ATR crystal include zinc selenide, germanium and diamond. The IR beam enters the ATR crystal at a certain angle (approx. 45°) and is totally reflected at the interface of the sample. The fraction of the IR beam that penetrates into the sample is called evanescent wave. This wave will be attenuated when the sample absorbs energy in some spectral regions. After one or several internal reflections, the IR beam exits the ATR crystal and is collected by the IR-detector.

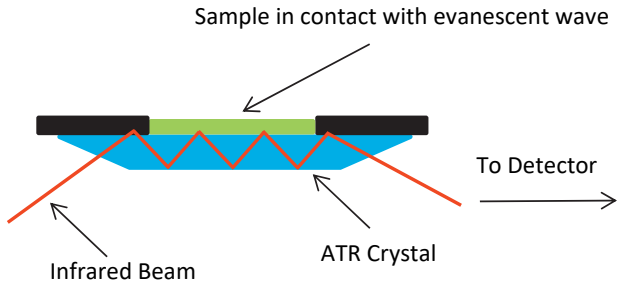


Fig. 14 Graphical representation of attenuated total reflection set-up

# 5. RESULTS AND DISCUSSION

This chapter summarizes the main results from the experimental work of ***Paper I-IV***, and some additional data are also presented. More detailed experimental conditions and discussions related to the results can be found at the end of this thesis in ***Paper I-IV***.

## 5.1. Acid-base characterization of zeolites

### 5.1.1. Potentiometric acid-base titration

A specific potentiometric acid-base titration method was used to characterize the acidity of zeolites in aqueous solution. This research can help us to have a better understanding of the catalytic property of zeolites in aqueous phase reactions and also the role of the acid groups in electrochemical synthesis of PPy/zeolite composites.

Except the silica mesoporous material Si-MCM-48, the other titrated zeolites are in the protonated form. Accurately weighed zeolite powder (approximately 0.85 g) suspended in 150 mL of 0.1 M $NaNO_3$ solution was titrated by stepwise additions of the titrant (0.1 NaOH + 0.1 $NaNO_3$) under argon atmosphere. The obtained titration curves (pH vs. $V_{OH^-}$, volume of added NaOH) of the zeolites in ***Paper I, III and IV*** are shown in Fig. 15. From the shapes of these curves it can be seen that all the titrated zeolites are acidic materials and contain various acid groups in their frameworks. It should be noted that due to some side reactions observed on the titration curve of H-Beta-300 in the alkaline range (pH > 10), it is suggested to stop the titration when the pH of the titrated suspension reaches ca pH 10.

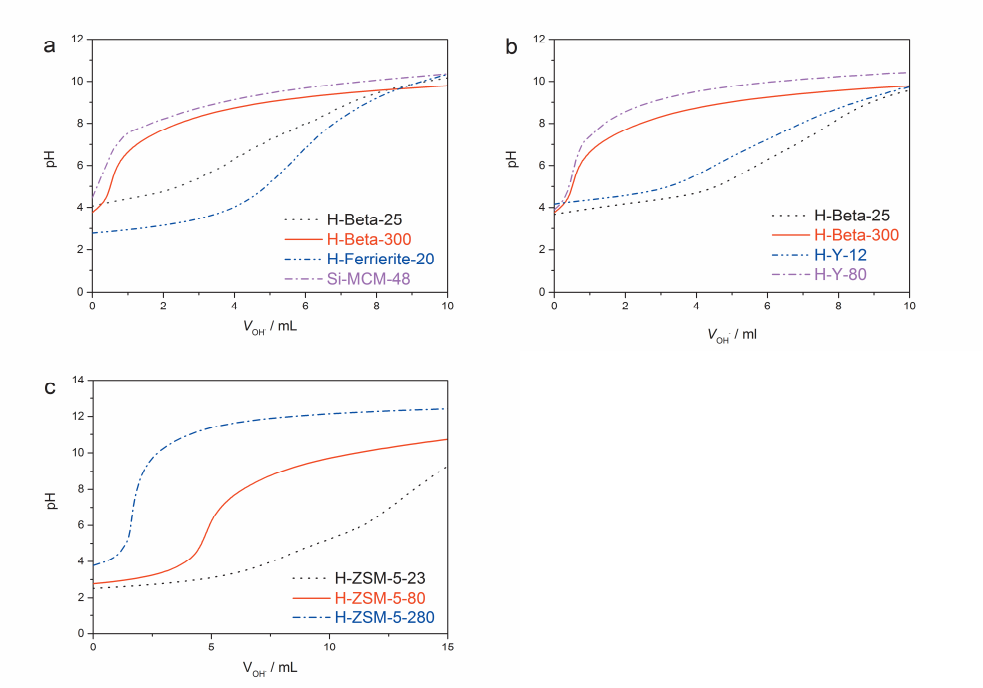


Fig. 15 Potentiometric titration curves of the studied pristine zeolites in a) ***Paper I, Fig. 3***, b) ***Paper III, Fig. 2***, and c) ***Paper IV, Fig. 1***

The protonation constants as well as the concentrations of the acid groups in the zeolites are given after evaluation of the titration data by the Gran method. Due to the weak acidity of the zeolites, the function $f_3(V) = K \cdot 10^{-pH} \cdot V$ in Table 2 was used in the calculations. Only the results from ***Paper I*** are presented in Table 3. Depending on the lg$K$ values, these acid groups are separated into two categories: moderate acid group and weak acid group. The moderate acid group, defined when its lg$K \leq 6.0$, is formed due to OH bridging of a framework silicon to a framework aluminum. The weak acid group, defined when its lg$K > 6.0$, is formed due to the dehydroxylation of alumina hydrates into transition alumina generating coordinately unsaturated sites [100]. In other words, the moderate and weak acid groups can be viewed as the Brønsted and Lewis acid groups, respectively. It can be seen in Table 3 that both H-Beta-25 and H-Beta-300 contain one moderate acid group ($R_1^- H^+$) and two weak acid groups ($R_2^- H^+$ and $R_3^- H^+$), while H-Ferrierite-20 has two moderate acid groups ($R_1^- H^+$ and $R_2^- H^+$) and two weak acid

groups ($R_3^-H^+$ and $R_4^-H^+$). Due to the absence of aluminum in Si-MCM-48, only one weak acid group ($R_3^-H^+$) was found in its framework. The strongest acid group is found in H-Ferrierite-20 with the lg$K$ value of 3.1 and concentration of 580 μmol/g. H-Ferrierite-20 also contains another type of moderate acid group $R_2^-H^+$ (lg$K$ = 5.3 and concentration = 130 μmol/g), indicating that another tetrahedrally coordinated aluminum species exists in this zeolite. Similar lg$K$ values of $R_1^-H^+$ are found in both H-Beta-25 and H-Beta-300 zeolites, meaning that these acid groups are identical. On the other hand, the different lg$K$ values of $R_1^-H^+$ in the Beta zeolites and in the H-Ferrierite-20 zeolite is the sign that the aluminum atoms creating these two moderate acid groups are in different frameworks. In their classical paper on the acid properties of silicates, Schinler and Kamber give lg$K$ value of 6.8 for silicate [101]. Iler gives additional lg$K$ values for silicate structures: 8.0 − 10.7 [102]. Similar values for the materials studied in this work were found in Table 3 and it can be concluded that these acid groups are due to the silicate structure in the materials and can be referred as the Lewis acid groups.

Table 3 also presents the results obtained by using the computer program FITEQL. A model with three acid groups gave the best fit to the experimental data for the H-Beta-25 and H-Beta-300, and a model with one acid group was the best for Si-MCM-48. For H-Ferrierite-20, however, the result with a four acid group model was more accurate. As can be seen, the Gran method gives similar results as the FITEQL program, indicating the reliability of these values and both methods can be used to evaluate the potentiometric titration data of the zeolites.

Table 3 Protonation constants (lg*K*) and concentrations (*c* μmol/g) of acid groups in the pristine zeolites H-Beta-25, H-Beta-300, H-Ferrierite-20, and Si-MCM-48 determined by the FITEQL and Gran methods (***Table 2, Paper I***)

| | **H-Beta-25** | | | | **H-Beta-300** | | | |
|---|---|---|---|---|---|---|---|---|
| | **FITEQL** | | **Gran** | | **FITEQL** | | **Gran** | |
| **Acid groups** | **lg*K*** | ***c*** **(μmol/g)** | **lg*K*** | ***c*** **(μmol/g)** | **lg*K*** | ***c*** **(μmol/g)** | **lg*K*** | ***c*** **(μmol/g)** |
| $R_1^-H^+$ | 4.5 | 570 | 4.6 | 520 | 4.1 | 90 | 4.0 | 110 |
| $R_2^-H^+$ | 6.3 | 230 | 6.1 | 230 | 6.9 | 180 | 6.8 | 190 |
| $R_3^-H^+$ | 8.2 | 270 | 8.0 | 290 | 8.3 | 380 | 8.2 | 370 |
| **Total** | | 1070 | | 1040 | | 650 | | 670 |
| | **H-Ferrierite-20** | | | | **Si-MCM-48** | | | |
| | **FITEQL** | | **Gran** | | **FITEQL** | | **Gran** | |
| **Acid groups** | **lg*K*** | ***c*** **(μmol/g)** | **lg*K*** | ***c*** **(μmol/g)** | **lg*K*** | ***c*** **(μmol/g)** | **lg*K*** | ***c*** **(μmol/g)** |
| $R_1^-H^+$ | 3.0 | 600 | 3.1 | 580 | | | | |
| $R_2^-H^+$ | 5.5 | 120 | 5.3 | 130 | | | | |
| $R_3^-H^+$ | 6.7 | 170 | 6.6 | 180 | 8.1 | 270 | 8.0 | 280 |
| $R_4^-H^+$ | 8.5 | 200 | 8.4 | 210 | | | | |
| **Total** | | 1090 | | 1100 | | 270 | | 280 |

### 5.1.2. Characterization of the titrated zeolites

At the same time, the acidity of H-Beta-25, H-Beta-300, H-Ferrierite-20 and Si-MCM-48 were studied by FTIR using pyridine as the test molecule, and the results are compared with their pristine forms [103, 104]. As can be seen in Table 4, the concentration of the acid groups determined by the FTIR-pyridine method is much lower in the same zeolite than when determined by the potentiometric titration method (Table 3). Since the potentiometric titration was done in an aqueous solution at 25 ℃ compared with the FTIR-pyridine method done in gaseous phase at elevated temperatures (250 – 450℃), it is obvious that different values are obtained. In addition, some of the acid groups in the Ferrierite-20 framework may not be accessible to the large pyridine molecules during the FTIR experiments. However, the small size of $OH^-$ ions makes it easy for them to penetrate into the small pores of Ferrierite-20.

In the titrated zeolites, the Brønsted acid groups were neutralized during the titration, and therefore the FTIR pyridine method did not show any of these sites. Lewis acid groups, however, were detected in the titrated H-Beta-25 but at lower concentrations than in the pristine zeolites. In the other titrated zeolites, all the Lewis sites were neutralized.

Table 4 Concentrations of Brønsted acid groups (BAS) and Lewis acid groups (LAS) in the pristine and the titrated zeolites determined by FTIR-pyridine method (***Table 3, Paper I***)

| | $c_{BAS}$ (µmol/g) | | | $c_{LAS}$ (µmol/g) | | | **Total concentration (µmol/g)** |
|---|---|---|---|---|---|---|---|
| **Zeolites** | **250** ℃ | **350** ℃ | **450** ℃ | **250** ℃ | **350** ℃ | **450** ℃ | |
| Pristine H-Beta-25 [36] | 219 | 187 | 125 | 82 | 43 | 25 | 301 |
| Titrated H-Beta-25 | 0 | 0 | 0 | 55 | 11 | 9 | 55 |
| Pristine H-Beta-300 [36] | 54 | 49 | 23 | 28 | 9 | 4 | 82 |
| Titrated H-Beta-300 | 0 | 0 | 0 | 0 | 0 | 0 | 0 |
| Pristine H-Ferrierite-20 [37] | 349 | 339 | 275 | 8 | 4 | 2 | 357 |
| Titrated H-Ferrierite-20 | 0 | 0 | 0 | 0 | 0 | 0 | 0 |
| Pristine Si-MCM-48 | 0 | 0 | 0 | 12 | 3 | 0 | 12 |
| Titrated Si-MCM-48 | 0 | 0 | 0 | 3 | 0 | 0 | 3 |

The X-ray diffraction (XRD) patterns of the pristine zeolites as well as the titrated ones are shown in Fig. 16. As can be seen, all the titrated zeolites kept the main structural integrity intact compared with their pristine state, indicating that the base (NaOH) used in the titration did not destroy the main crystal structure of the zeolites. The interaction of $H_2O$ molecules with the Brønsted and Lewis acid groups have been studied in detail in refs [105, 106]

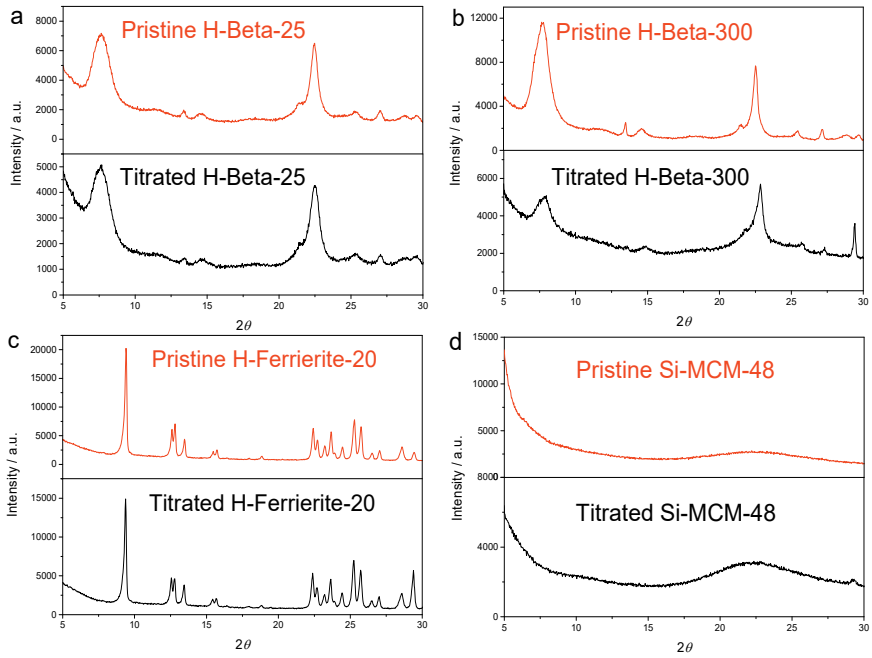


Fig. 16 XRD patterns of the pristine and titrated a) H-Beta-25, b) H-Beta-300, c) H-Ferrierite-20, and d) Si-MCM-48 (***Fig. 5, Paper I***)

Since aluminum (Al) and silicon (Si) are the key components in forming the Brønsted and Lewis acid groups, the ICP-OES technique was used to determine their concentrations in the pristine as well as in the titrated zeolites. Table 5 only gives the results for Al. Assuming that every Al atom in the tetrahedral framework creates a Brønsted acid group, the theoretical concentration of the Brønsted acid groups in the pristine zeolites should be the same as the concentration of Al in them as given in Table 5. The experimentally determined total concentration of the Brønsted acid groups can be calculated by combining the concentrations of the acid groups whose lg*K* values are < 6.0 from Table 3. Those values are also included in Table 5. As can be seen, the theoretical and the experimentally observed concentrations of the Brønsted acid groups in the pristine zeolites differ from each other to some extent: 1000 μmol/g vs. 520 μmol/g (H-Beta-25), 150 μmol/g vs. 110 μmol/g (H-Beta-300), and 1260 μmol/g vs. 710 μmol/g (H-Ferrierite-20). This

indicates that most of the Al in H-Beta-300 contributes to the Brønsted acid groups, but approximately 48% of Al in H-Beta-25 and 44% of aluminum in H-Ferrierite-20 are located in the extra framework. Concentrations of the Brønsted acid groups determined by the FTIR-pyridine method from Table 4 are also included in Table 5. In general, the proposed titration method gives the results that are ca 50-55% higher than the values obtained with the FTIR-pyridine method, and this can be explained by restricted accessibility of pyridine.

Table 5 Concentrations of Al in pristine and titrated zeolites determined by ICP-OES, and concentrations of Brønsted acid groups (BAS) determined by titration and FTIR-pyridine methods (***Table 4, Paper I***)

| **Zeolites** | $c_{Al}$ **by ICP-OES (μmol/g)** | $c_{BAS}$ **by titration (μmol/g)** | $c_{BAS}$ **by FTIR-pyridine (μmol/g)** | $\frac{c_{BAS}\text{FTIR-pyridine}}{c_{BAS}\text{Titration}}$ |
|---|---|---|---|---|
| Pristine H-Beta-25 | 1000 | 520 | 291 | 55% |
| Titrated H-Beta-25 | 860 | 0 | 0 | |
| Pristine H-Beta-300 | 150 | 110 | 54 | 49% |
| Titrated H-Beta-300 | 110 | 0 | 0 | |
| Pristine H-Ferrierite-20 | 1260 | 710 | 349 | 49% |
| Titrated H-Ferrierite-20 | 1000 | 0 | 0 | |
| Pristine Si-MCM-48 | 0 | 0 | 0 | |
| Titrated Si-MCM-48 | 0 | | | |

Also in Table 5, the titrated zeolites contain a lower concentration of Al than their pristine states, meaning that some aluminum was dissolved from zeolite during the titration. Approximately 260 μmol/g of Al dissolved from H-Ferriertie-20 during the titration, and this amount is higher than H-Beta-25 (140 μmol/g) and H-Beta-300 (40 μmol/g). However, the cause of this release is unknown. Therefore, additional ICP-OES measurement has been done in order to determine the dissolved Al and Si when the zeolite was dispersed in deionized water. The results are shown in Fig. 17 (observe the different scales in Fig. 17). The amount of dissolved Al and Si only slightly increased with the stirring time for the three zeolites. More Al is found than Si, implying that part of the Al may not have been bonded in the framework or part of the Al framework is not stable in water. H-Beta-25 solution contains a higher concentration of Al compared with that of H-Beta-300 due to the high content of Al in H-Beta-25 (Table 5). However, although H-Ferrierite-20 contains more Al than that of H-Beta-25, a lower concentration of Al and Si is detected in H-Ferrierite-20 solution. This study indicates that the structure of the zeolite can influence the

stability of the Al and Si framework, but the acid-base reaction can cause more Al to dissolve from zeolites, especially when the zeolite contains a high concentration of Al, e.g. H-Ferrierite-20.

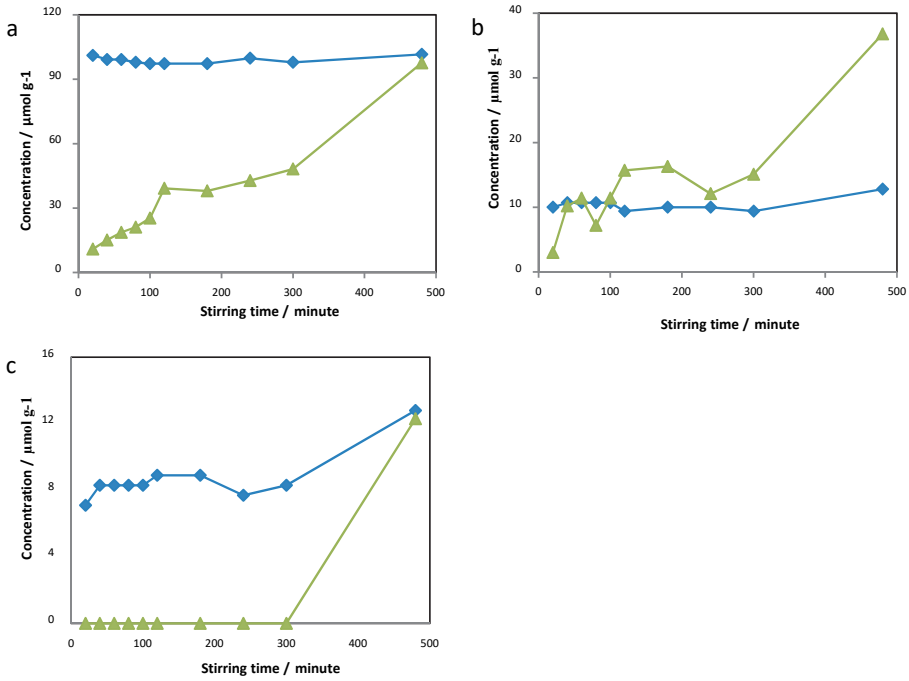


Fig. 17 Concentrations of dissolved aluminum and silicon determined by the ICP-OES technique in various zeolites suspensions, a) H-Beta-25, b) H-Beta-300, and c) H-Ferrierite-20. ◆ is attributed to the dissolved aluminum and ▲ is the dissolved silicon

$^{27}$Al MAS NMR spectroscopy was used to characterize the coordination states of aluminum in both pristine and titrated zeolites. As shown in Fig. 18, two representative NMR peaks around 55 ($Al^{IV}$) and 0 ($Al^{VI}$) ppm are observed on the $^{27}$Al NMR spectra of pristine H-Beta-25, H-Beta-300 and H-Ferrierite-20 in Fig. 18a, b and c, respectively. The resonance peak at 55 ppm with very strong intensity is attributed to the Al sites on the tetrahedral framework, and the peak at 0 ppm with very low intensity is assigned to the octahedral non-framework Al sites [107, 108]. Only the $Al^{IV}$ peak can be found in the $^{27}$Al NMR spectra of the titrated H-Beta-25, H-Beta-300 and H-Ferrierite-20, indicating that the tetrahedral Al sites attributed to the zeolite framework are maintained while the octahedral Al sites are broken after the titration. In other words, the

tetrahedral framework Al is much more stable than the octahedral non-framework Al in the alkaline environment. There is no Al peak observed in the $^{27}$Al NMR spectra of Si-MCM-48 in Fig. 18d due to the absence of aluminum in this zeolite.

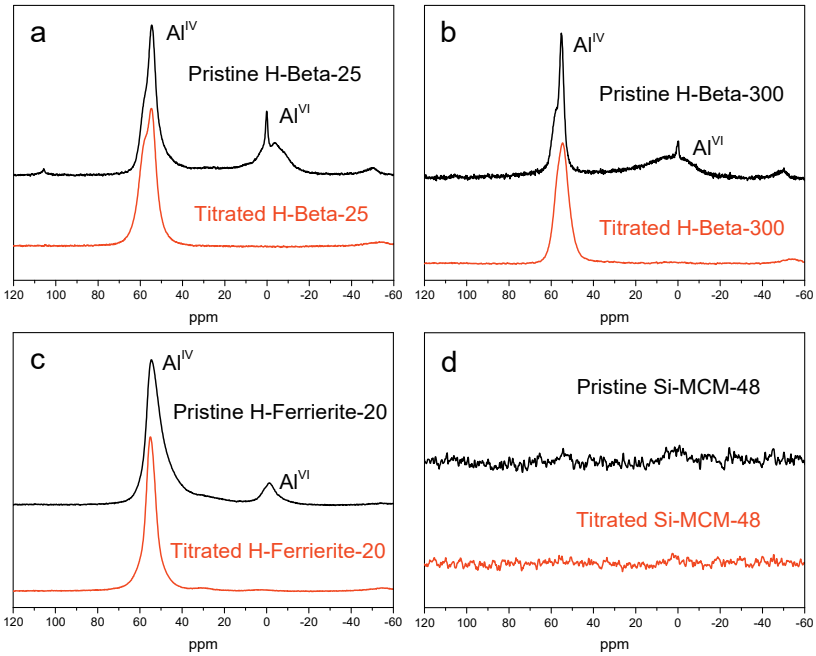


Fig. 18 $^{27}$Al MAS NMR spectra of the pristine and titrated zeolites a) H-Beta-25, b) H-Beta-300, c) H-Ferrierite-20 and d) Si-MCM-48 (***Fig. 6, Paper I***)

As the results mentioned above, the acidic OH groups in the studied zeolites were completely neutralized after the potentiometric titration. Although a small amount of aluminum and silicon were found to leach out from the zeolite during the titration, the structures of the titrated zeolites are still maintained. This is also indicating that the titrant is mainly contributing to the acid-base reaction instead of to other unexpected reactions. The Al remains in the titrated zeolites is attributed to the tetrahedral framework Al$^{IV}$.

## 5.2. Synthesis and characterization of polypyrrole/zeolite composites

### 5.2.1. Chemical synthesis and characterization of polypyrrole/zeolite composites

In this thesis work, the polypyrrole/zeolite (PPy/zeolite) composites were first synthesized by using chemical polymerization. The protonated form of Beta zeolites with Si/Al ratios of 25, 150 and 300 were selected as the host materials. Various amounts of pyrrole monomer, 1.0, 2.0 and 3.0 mL, were polymerized with 1.0 g zeolite powder suspended in 100 mL water. $FeCl_3$ was used as the oxidizing agent in the reaction and the exact amount of $FeCl_3$ selected for the reaction can be found in ***Table 1***, ***Paper II***. The schematic presentation of the formation of the nanocomposite PPy/H-Beta-zeolite is given in Eq. 5, where PPy is doped both with $Cl^-$ and the anionic groups $(SiOAl)^-$ in the zeolite framework. The composites synthesized were filtrated and washed, and are denoted as 1, 2, 3 mL PPy/H-Beta zeolites.

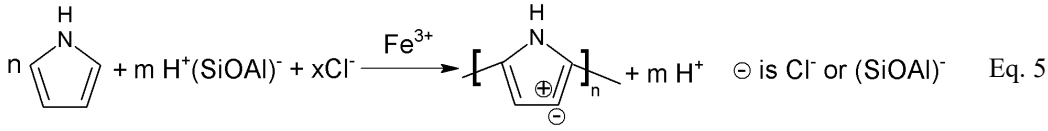


Eq. 5

H-Beta zeolites belong to microporous materials which have high surface area and micropore volume. However, incorporation of PPy significantly decreased their surface area and the micropore volume (Table 6). With increasing amount of pyrrole monomer in the synthesis reaction, the surface area and the micropore volume of the Beta zeolites decreased. Therefore, the channels of H-Beta zeolite are considered to be occupied by PPy and the outer surface of the zeolite powder can be regarded to be covered by the PPy layer.

Also in Table 6, the electrical conductivities of PPy/H-Beta-25, PPy/H-Beta-150 and PPy/H-Beta-300 are compared with the pristine ones as well as with the PPy($Cl^-$) which was synthesized in the same way. Obviously, the H-Beta zeolite is an insulator. When PPy was introduced into the zeolite framework, the conductivity of the zeolite was changed from insulator to conductor and further to semiconductor. The conductivities of the composites with 1 mL loading are approximately the same as the conductivity of PPy($Cl^-$). Composites with 2 mL loading, however, exhibit about ten times higher conductivity, indicating better alignment of the polymer chains in

the composites than in PPy($Cl^-$). When the loading is further increased to 3 mL, conductivity drops, as can also be seen in 3 mL PPy($Cl^-$), and such a low electrical conductivity may be e.g. due to a high degree of cross linking in the polymer. However, 3 mL PPy/H-Beta composites show a much higher conductivity than those of 3 mL PPy($Cl^-$). This may be due to the well-ordered framework structure of the zeolites, where PPy is located inside or on the surface, thereby decreasing the cross-linking of the PPy chain.

With the same loading amount of pyrrole monomer, PPy/H-Beta-300 composite exhibits slightly lower electrical conductivity than the composites with H-Beta-25 and H-Beta-150, indicating that a high Si/Al ratio of the host zeolite seems to have a negative effect on the electrical conductivity of the polymer/zeolite composite.

Table 6 Surface area, micropore volume and electrical conductivity of pristine H-Beta zeolites, the PPy/H-Beta composites and the PPy($Cl^-$) (***Table 2, Paper II***)

| Sample | Surface area ($m^2/g$) | Micropore volume ($\times 10^{-3}$ $cm^3/g$) | Conductivity (S/cm) |
|---|---|---|---|
| H-Beta-25 | 520 | 185 | $5.4\times10^{-9}$ |
| 1 mL PPy/H-Beta-25 | 94 | 33 | $8.2\times10^{-1}$ |
| 2 mL PPy/H-Beta-25 | 45 | 16 | $1.2\times10^{0}$ |
| 3 mL PPy/H-Beta-25 | 25 | 9 | $2.0\times10^{-1}$ |
| H-Beta-150 | 509 | 181 | $5.0\times10^{-9}$ |
| 1 mL PPy/H-Beta-150 | 134 | 48 | $1.3\times10^{0}$ |
| 2 mL PPy/H-Beta-150 | 21 | 6 | $1.1\times10^{0}$ |
| 3 mL PPy/H-Beta-150 | 28 | 6 | $1.4\times10^{-2}$ |
| H-Beta-300 | 460 | 163 | $7.1\times10^{-9}$ |
| 1 mL PPy/H-Beta-300 | 52 | 19 | $6.7\times10^{-1}$ |
| 2 mL PPy/H-Beta-300 | 24 | 9 | $7.7\times10^{-1}$ |
| 3 mL PPy/H-Beta-300 | 26 | 9 | $6.2\times10^{-6}$ |
| 1 mL pure PPy($Cl^-$) | | | $9.7\times10^{-1}$ |
| 2 mL pure PPy($Cl^-$) | | | $1.0\times10^{-1}$ |
| 3 mL pure PPy($Cl^-$) | | | $6.1\times10^{-8}$ |

The distribution of PPy in the host zeolite was studied by Transmission Electron Microscopy (TEM). The channels in the H-Beta-25 structure are observed in Fig. 19a, and the morphology of the PPy/H-Beta-25 composite with different magnifications is shown in Fig. 19b and c. No separate zeolite nanoparticles or separate PPy clusters are observable, but the host zeolite nanoparticles are rather entrapped inside the PPy clusters. The black dots, marked by the arrows

in Fig. 19c and d, belong to the PPy chains that may have been formed inside the channels of H-Beta-25. Furthermore, the decreased surface area and the micropore volume obtained for PPy/H-Beta-25, PPy/H-Beta-150 and PPy/H-Beta-300 compared with pristine H-Beta-25, H-Beta-150 and H-Beta-300 (Table 6) can be taken as a confirmation of the formation of PPy in the channels of the H-Beta zeolites. In addition, the well-ordered uniform porous structure indicates that introduction of PPy into the channels will not destroy the zeolite structure.

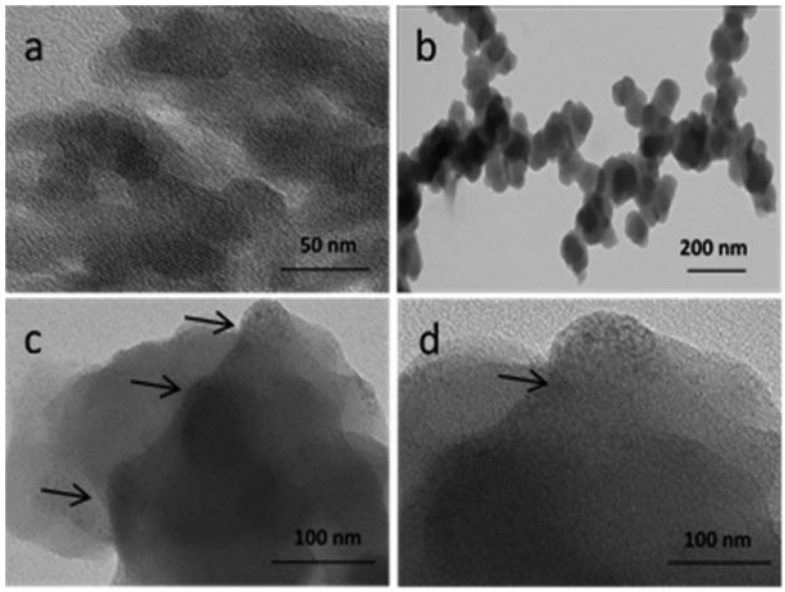


Fig. 19 Transmission electron micrographs of a) H-Beta-25, b), c) and d) 1 mL PPy/H-Beta-25 composite (***Fig. 3, Paper II***)

### 5.2.2. Electrochemical synthesis and characterization of polypyrrole/zeolite composites

In addition to chemical synthesis, polypyrrole/zeolite (PPy/zeolite) composites were also obtained by using electrochemical polymerization. Potential cycling as well as the method of constant potential were used for electrodeposition. It was, however, found that the PPy/zeolite composites can only be obtained by applying a constant potential to the electrode. The protonated form of Beta zeolites with $SiO_2/Al_2O_3$ ratios of 25 and 300 and Y zeolites with $SiO_2/Al_2O_3$ ratios of 12 and 80 were used for this research. The reaction was performed in aqueous solution

containing pyrrole monomer and zeolite powders. The anionic groups in the zeolites framework functioned as the counter ions for PPy, as indicated in Eq. 6.

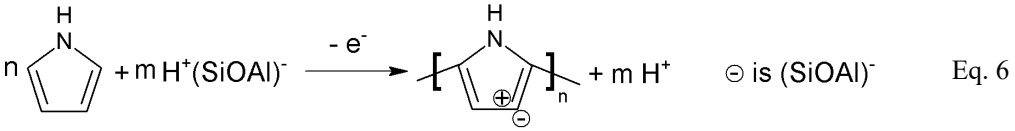


Eq. 6

Prior to the electrochemical synthesis, the concentrations and the protonation constants of the anionic groups in these zeolites were determined by potentiometric titration and the Gran method. The titration curves have been shown in Fig. 15b. From the results one can find that Beta and Y zeolites contain various anionic groups and, thus, influence the electrochemical properties of the PPy/zeolite composite.

The electrochemical behaviors of PPy/zeolite composites deposited on platinum (Pt) were studied by cyclic voltammetry in 0.1 M NaCl electrolyte solution containing 1 mM $Ru(NH_3)_6Cl_3$ as redox couple. The obtained cyclic voltammograms were compared with that of PPy doped with chloride ($PPy(Cl^-)$) and the bare Pt electrode. The cyclic voltammograms of the redox system $[Ru(NH_3)_6]^{2+}/[Ru(NH_3)_6]^{3+}$ in Fig. 20 show well-developed redox peaks at all electrodes under investigation. The peak separation $\Delta E^P$ (difference between oxidation and reduction peak) of the redox couple at the PPy/H-Beta-25, PPy/H-12, and PPy/H-Y-80 composite electrodes are approximately the same. However, at the PPy/H-Beta-300, the $\Delta E^P$ is three times larger indicating a slow electron transfer at that substrate. The PPy/H-Beta-300 composite contains also the lowest amount of PPy, which definitely affects the electrochemical behavior of the redox couple at that substrate. In addition, the cyclic voltammograms in Fig. 20 clearly show that the charge transfer reaction combined with the redox couple during potential cycling takes place at the surface of the composite and not at the underlying Pt substrate indicating a full coverage of the Pt substrate by the composites.

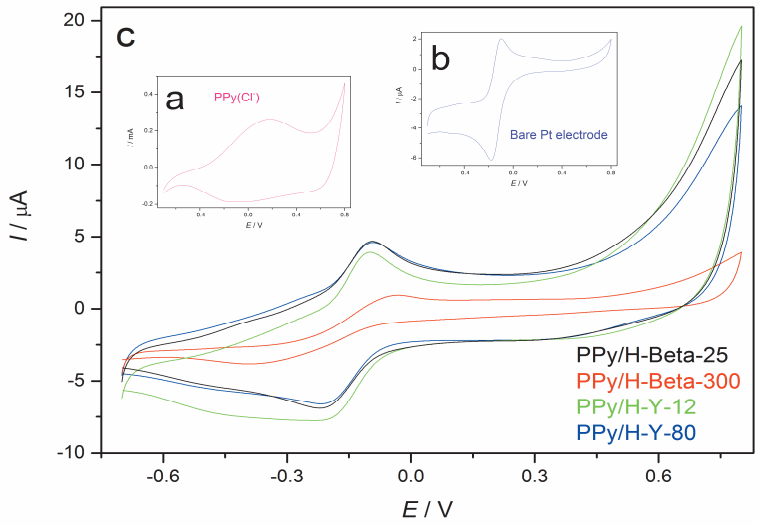


Fig. 20 Cyclic voltammograms of a) PPy($Cl^-$) and b) Bare Pt electrode, c) PPy/zeolite composite films on Pt electrode in 1 mM $Ru(NH_3)_6^{3+}$ and 0.1 M NaCl solution in the potential range -0.7 to +0.8 V with scan rate of 5 mV/s (***Fig. 5, Paper III***)

The electrochemical behavior of the PPy/zeolite composites synthesized on indium tin oxide glass (ITO) were characterized in 0.1 M NaCl solution and the cyclic voltammograms are shown in Fig. 21. The following reaction (Eq. 7) may be proposed to describe the electrochemical behavior of PPy/zeolite composites, i.e. the doping/dedoping reaction:

$$PPy^+ e^-{\cdot}Z^-{\cdot}C^+ \underset{red}{\overset{ox}{\rightleftharpoons}} PPy^+{\cdot}Z^- + e^- + C^+ \qquad \text{Eq. 7}$$

where $PPy^+e^-$ denotes the electrically neutral polymer. $Z^-$ is the anionic group in the zeolite framework and $C^+$ is a cation required to balance the electroneutrality. $Z^-$ is immobile and the electron transfer is balanced by the movement of the cation $C^+$.

As can be seen in Fig. 21, PPy/H-Beta composites show cyclic voltammograms that are very similar to PPy($Cl^-$) in the same electrolyte. The PPy/H-Y composites, however, show outdrawn cyclic voltammograms indicating a slow electron transfer during the redox reaction of the polymer.

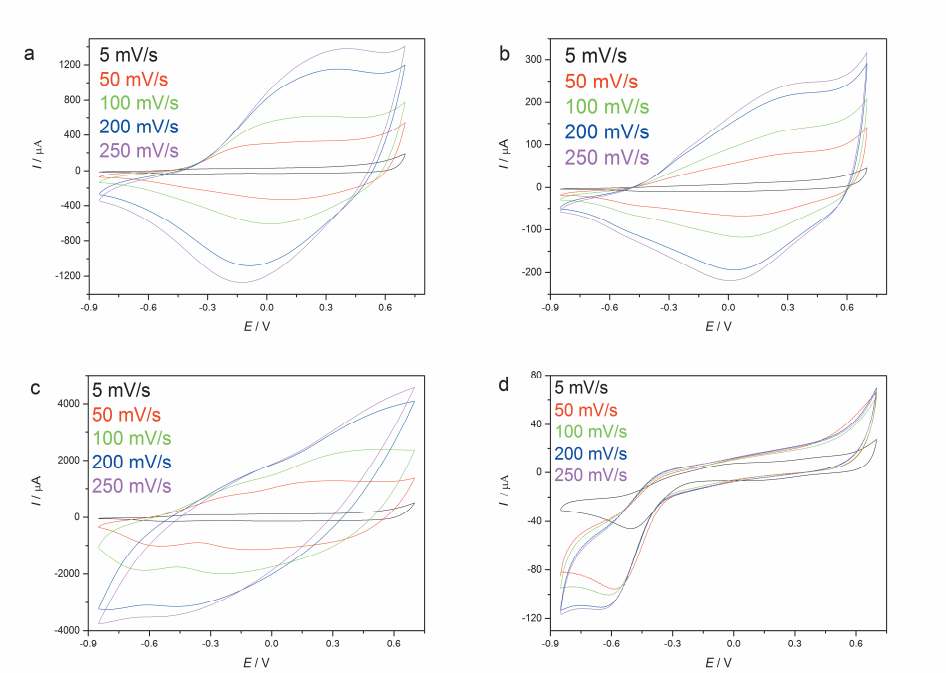


Fig. 21 Cyclic voltammograms of a) PPy/H-Beta-25, b) PPy/H-Beta-300, c) PPy/H-Y-12 and d) PPy/H-Y-80 composite films on ITO electrode in 0.1 M NaCl solution at potential range -0.85 to +0.7 V with scan rates of 5, 50, 100, 200 and 250 mV $s^{-1}$ (***Fig. 3, Paper III***)

The morphology of the PPy/zeolite composites and PPy($Cl^-$) synthesized on the Pt electrode as well as the host zeolites were observed with scanning electron microscopy (SEM). The images of PPy($Cl^-$) and the H-Y-12 zeolite, together with the composite PPy/H-Y-12, are shown in Fig. 22. Typical images for PPy($Cl^-$) and the H-Y-12 zeolite can be seen in Fig. 22a and Fig. 22b, respectively. Fig. 22c shows that the PPy/H-Y-12 composite film is composed of zeolite particles and PPy. The zeolite particles are observable on the surface of the composite but are obviously also embedded in the layer of PPy, resulting in an uneven surface of the composite. A magnification image of PPy/H-Y-12 composite (Fig. 22d) indicates that zeolite particles are covered by PPy.

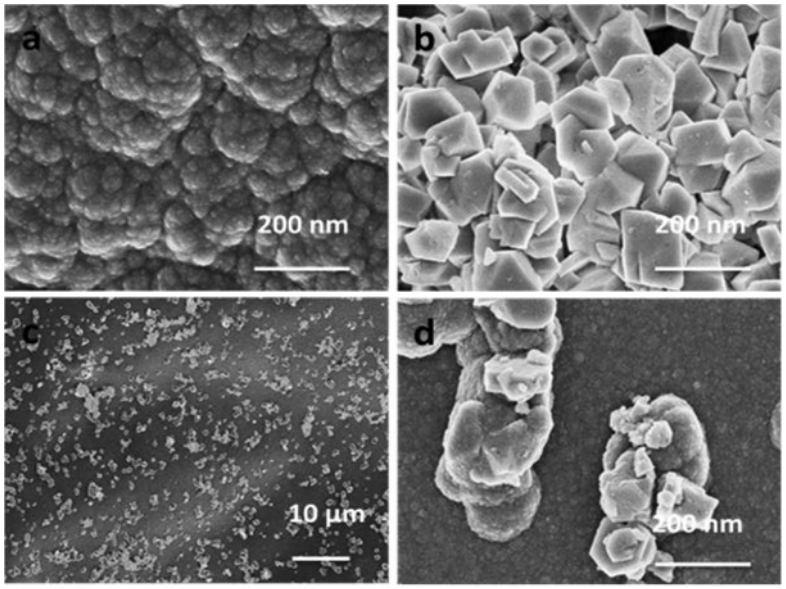


Fig. 22 Scanning electron micrographs of a) PPy($Cl^-$) film (200 nm), b) H-Y-12 zeolite (200 nm), c) PPy/H-Y-12 (10 µm) and d) PPy/H-Y-12 (200 nm) composite film synthesized on Pt electrode by constant potential method (***Fig. 7, Paper III***)

The thickness of the PPy/zeolite composite films deposited on the ITO substrate was measured by SEM as well. The cross-section images of the composite films are shown in Fig. 23. A distinct layer of the composite, marked with a green line, is evident in each micrograph. It can clearly be seen that the zeolite particles are not only present on the surface of the composite film but also embedded in the PPy. Due to the fact that the anionic groups in the zeolite functioned as counter ion during electropolymerization, PPy was thus formed on the zeolite particles. The film thickness decreases in the sequence of PPy/H-Y-12 (1720 nm) > PPy/H-Beta-25 (840 nm) > PPy/H-Y-80 (410 nm) > PPy/H-Beta-300 (150 nm). The charges consumed in the polymerization reaction, naturally, also follow the same sequence: PPy/H-Y-12 (351 mC)>PPy/H-Beta-25 (215 mC) > PPy/H-Y-80 (86 mC) > PPy/H-Beta-300 (42 mC). Since each composite was prepared with exactly the same reaction parameters, i.e. the applied potential, reaction time and particle size of zeolite, the sequence is determined by the concentration of the anionic groups of the host zeolite (see ***Table 2 in Paper III***). This indicates that the electropolymerization of PPy

propagated more efficiently with the zeolite which contains higher concentration of anionic groups, and therefore generating a thicker composite film. However, the magnitudes of the recorded currents (Fig. 21) show that the electropolymerization did not follow the patterns of the thickness of the composite film PPy/H-Y-12 > PPy/H-Beta-25 > PPy/H-Beta-300 > PPy/H-Y-80, indicating that the physical-chemical and structural properties of the host zeolite also influenced the electrochemical behavior of the PPy/zeolite composite.

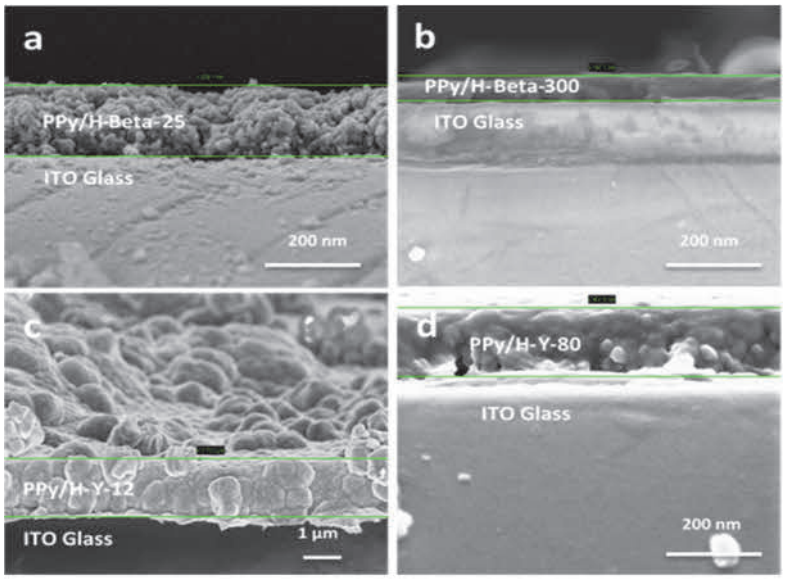


Fig. 23 Scanning electron micrographs of the cross-section of a) PPy/H-Beta-25 (200 nm), b) PPy/H-Beta-300 (200 nm), c) PPy/H-Y-12 (1 µm) and d) PPy/H-Y-80 (200 nm) composite film synthesized on ITO electrode by constant potential method. The film is marked with the green line (***Fig. 6, Paper III***)

The FTIR-ATR reflection spectrum in the region from 1800 to 700 $cm^{-1}$ for PPy($Cl^-$) and the PPy/zeolite composites on Pt substrate, and also the spectrum of the pristine zeolites are shown in Fig. 24. In the H-Beta-25 zeolite spectrum in Fig. 24a, the peaks at 1228, 1068 and 796 $cm^{-1}$ are assigned to the typical asymmetric and symmetric Si-O stretching vibrations [109]. On the other hand, the spectrum of PPy($Cl^-$) exhibits the characteristic absorption band of PPy at 1505 $cm^{-1}$ (C-C and C=C stretching vibrations), 1408 $cm^{-1}$ (C-N stretching vibration), 1255 $cm^{-1}$ (C-H or C-N in-plane vibration) and 1073 $cm^{-1}$ (C-H and N-H in-plane deformation vibrations) [110, 111].

These typical spectral features of PPy are also observable in the spectrum of the PPy/H-Beta-25 composite at slightly higher wavenumbers 1569, 1463, 1285 and 1078 $cm^{-1}$. Generally, the C-C band tends to shift to lower wavenumber as the conjugated length of the polymer is increased [112]. Thus, the conjugation length in the PPy/H-Beta-25 composite can be considered to be shorter than those in the PPy($Cl^-$). In addition, the absorption peaks at 1220 and 795 $cm^{-1}$ of the composite spectrum are attributed to the Si-O band from H-Beta-25 and another Si-O band at 1068 $cm^{-1}$ is overlapping with the C-H and N-H in-plane deformation vibrations (1073 $cm^{-1}$) of PPy. In the case of the PPy/H-Beta-300, PPy/H-Y-12 and PPy/H-Y-80 composites, both PPy bands and the bands of the zeolite can be observed in their respective FTIR-ATR reflection spectra. However, the various anionic groups present in the different zeolites cause the observed shift differences in the PPy absorption peaks.

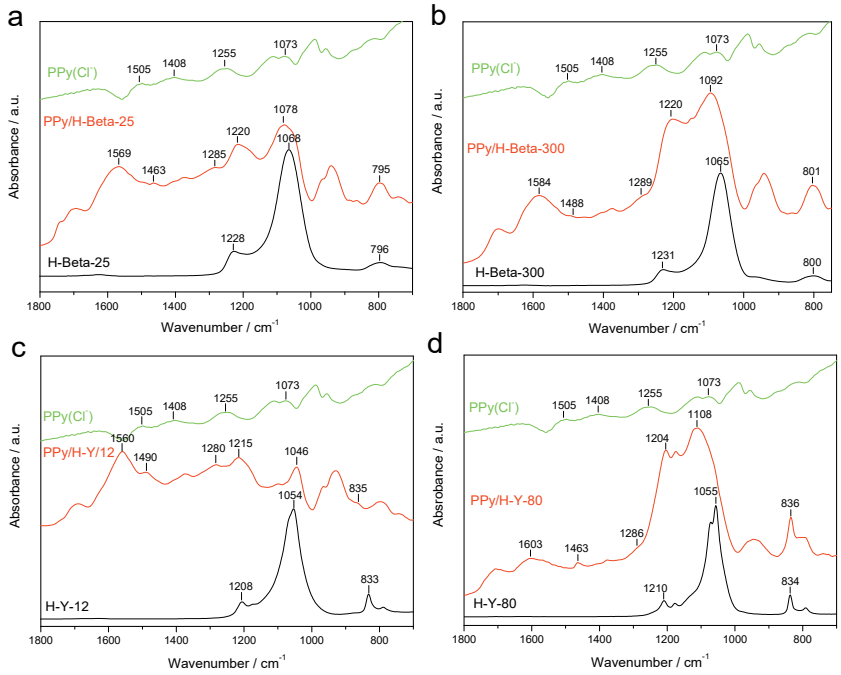


Fig. 24 FTIR-ATR spectra of a) PPy/H-Beta-25 composite, b) PPy/H-Beta-300 composite, c) PPy/H-Y-12 composite and d) PPy/H-Y-80 composite synthesized on Pt substrate (***Fig. 10, Paper III***)

### 5.3. Polypyrrole/zeolite composites as the solid contact in potassium ion-selective electrode

The polypyrrole/zeolite (PPy/zeolite) composites electrodeposited on the Pt substrate were applied and tested as the solid contact (SC) in a potassium ion-selective electrode ($K^+$-ISE). The selected host zeolites for PPy in this research include H-ZSM-5-23, H-ZSM-5-80 and H-ZSM-5-280. Polypyrrole/H-ZSM-5 solid-state potassium ion-selective electrodes were prepared by adding 40 µl of the potassium ion-selective-membrane (ISM) cocktail on the top of the composite.

The impedance measurements for the PPy($Cl^-$) and PPy/H-ZSM-5 composites were performed at the open-circuit dc-potential in 0.1 M KCl solution (frequency range = 10 mHz – 100 kHz, $\Delta E_{ac}$ = 5 mV). As shown in Fig. 25, the imaginary part of the impedance ($-Z''$) at low frequencies is ca four times higher in the spectrum of the PPy/zeolite composites film than in the spectrum of the PPy($Cl^-$) film, indicating that the redox capacitance of the composites is ca four times lower than that of PPy($Cl^-$). The inset window in Fig. 25 shows the high-frequency part of the impedance spectra of the PPy($Cl^-$) and the composite films, indicating that the PPy/zeolite composites have a higher resistance than PPy($Cl^-$). The poor redox capacitance and conductivity of the PPy/zeolite is obviously due to the insulating property and porosity of the zeolites, which decrease the electron/hole movement in such materials. The resistance of the composites increases in the order of PPy/H-ZSM-5-23 < PPy/H-ZSM-5-80 < PPy/H-ZSM-5-280, meaning that the zeolite which contains higher concentration of anionic groups can attract more PPy deposit on its framework and, thus, increase the conductivity of the composite.

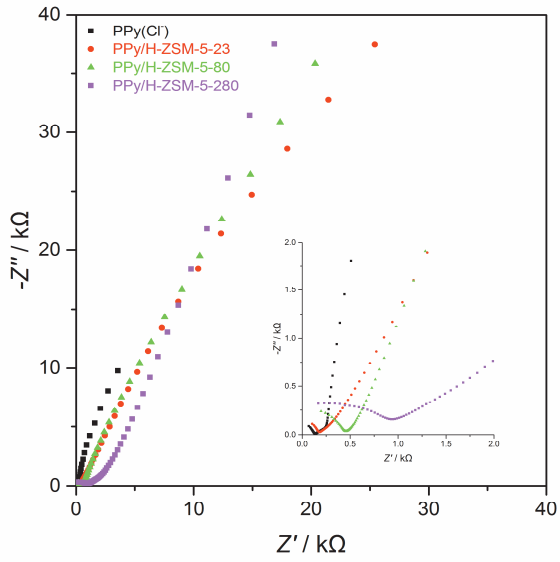


Fig. 25 Impedance spectra of PPy($Cl^-$) and PPy/zeolite film recorded at the open-circuit dc-potential in 0.1 M KCl solution, frequency range = 10 mHz – 100 kHz, $\Delta E_{ac}$ = 5 mV (***Fig. 6, Paper IV***)

A thin aqueous layer may be formed at the interface between the ISM and the SC regardless of the construction process, and thus counteract all the benefits of the SC [113]. Pretsch et al. proposed the potentiometric aqueous layer test to investigate the accumulation of such a layer [114]. In this research, all the electrodes were first exposed to a relatively high concentration (0.1 M) of the primary ion ($K^+$) for 1 hour, then to the same concentration of the interfering ion ($Na^+$) for 4 hours, and finally back to the primary ion solution for 4 hours. As can be seen in Fig. 26, the four prepared $K^+$-SC-ISEs show only a slight positive potential drift in the interfering ion ($Na^+$) solution and also when switched to the primary ion ($K^+$) solution, indicating that no aqueous layer was formed in the test. This implies that the PPy/zeolite composite has a similar hydrophobicity as PPy($Cl^-$). Hence, the hydrophobicity of the composite is determined mainly by PPy, rather than by the zeolite.

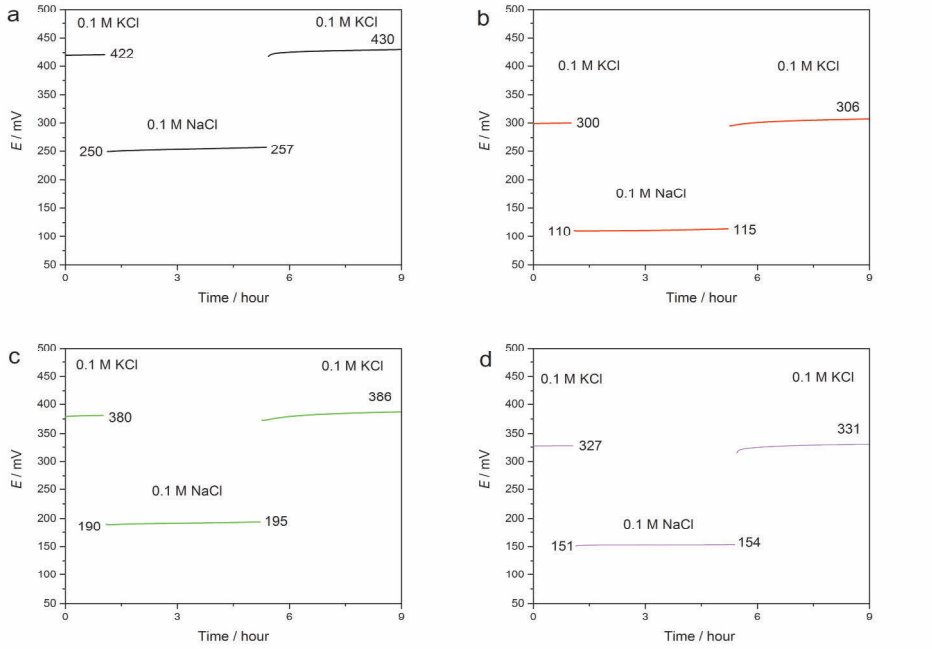


Fig. 26 Potentiometric aqueous layer test of a) PPy($Cl^-$), b) PPy/H-ZSM-5-23, c) PPy/H-ZSM-5-80 and d) PPy/H-ZSM-5-280 based $K^+$-ISEs (***Fig. 8, Paper IV***)

After equilibration in $10^{-3}$ M KCl solution for 2 days, the PPy($Cl^-$) and PPy/zeolite composite-based $K^+$-ISEs were calibrated in $10^{-2}$ – $10^{-7}$ M KCl solutions then back to $10^{-2}$ M. The obtained calibration curves are marked with A in Fig. 27. The low detection limit was determined by the intersection point of the extrapolated linear range and low concentration level segments of the calibration plot (IUPAC Recommendations) [115]. All the electrodes are sensitive to potassium ion with linear response in the activity range of $10^{-2}$ – $10^{-5}$ M. The slopes of the linear part on the calibration curves are 52.3 ± 0.3, 54.2 ± 0.4, 51.4 ± 0.2 and 52.8 ± 0.5 mV/decade for PPy($Cl^-$), PPy/H-ZSM-5-23, PPy/H-ZSM-5-80 and PPy/H-ZSM-5-280 based ISEs, respectively. The estimated low detection limit of the electrodes for $K^+$ ion is in the following order: PPy($Cl^-$) ((6.3 ± 0.7) × $10^{-6}$ M) < PPy/H-ZSM-5-23 ((7.1 ± 0.5) × $10^{-6}$ M) < PPy/H-ZSM-5-280 ((8.9 ± 0.9) × $10^{-6}$ M) < PPy/H-ZSM-5-80 ((9.7 ± 0.8) × $10^{-6}$ M). The standard deviation of the standard

potential values ($E^0$) of the $K^+$-ISE for PPy($Cl^-$) is ±2.2 mV, PPy/H-ZSM-5-23 is ±5.6 mV, PPy/H-ZSM-5-80 is ±10.6 mV, and PPy/H-ZSM-5-280 is ±17.7 mV.

After being conditioned in $10^{-3}$ M KCl solution for an additional 6 days, the same electrodes were calibrated again in the same way. The obtained calibration curves are marked with B in Fig. 27. As can be seen, the potentials of these electrodes were shifted to more positive values, which is 39 mV for PPy($Cl^-$), 45 mV for PPy/H-ZSM-5-23, 46 mV for PPy/H-ZSM-5-80 and 45 mV for PPy/H-ZSM-5-280. PPy($Cl^-$)-ISE exhibits the same linear activity range of $10^{-2}$ – $10^{-5}$ M. However, the PPy/zeolite-based ISEs show a linear response to $K^+$ in a broader activity range, i.e. $10^{-2}$ – $10^{-6}$ M. The slopes of the new linear part of the composite-based ISEs are 53.1 ± 0.2 mV/decade (PPy/H-ZSM-5-23), 52.1 ± 0.3 mV/decade (PPy/H-ZSM-5-80) and 52.7 ± 0.1 mV/decade (PPy/H-ZSM-5-280). The calculated low detection limit for the $K^+$ ion is as follows: PPy/H-ZSM-5-280 (1.0 ± 0.4) × $10^{-6}$ M < PPy/H-ZSM-5-80 (1.0 ± 0.6) × $10^{-6}$ M < PPy/H-ZSM-5-23 (2.1 ± 0.3) × $10^{-6}$ M < PPy($Cl^-$) (7.9 ± 0.5) × $10^{-6}$ M. The new standard deviation of $E^0$ values for the electrodes are ±2.0 mV (PPy($Cl^-$)), ±5.7 mV (PPy/H-ZSM-5-23), ±10.6 mV (PPy/H-ZSM-5-23) and ±17.6 mV (PPy/H-ZSM-5-23), respectively. Variations in the standard deviation of standard potential values between individual composite based ISEs is obviously due to the different zeolites in the composites. PPy/H-ZSM-5-23 has the highest amounts of anionic groups, contributing to the lowest standard deviation, whereas PPy/H-ZSM-5-280 contains the lowest amounts of anionic groups, contributing to the highest standard deviation. Additionally, the anionic groups are not homogeneously distributed in the structure of the zeolite, which may influence the PPy growth evenly on the zeolite frameworks, and thus influence the homogeneity of the composite and hence the performance of the electrode.

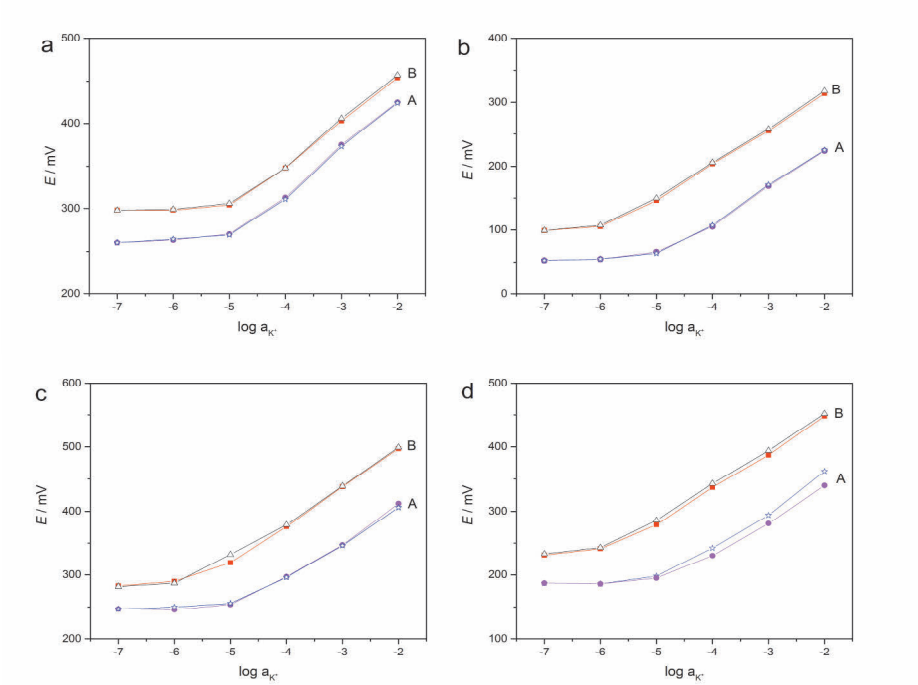


Fig. 27 Calibration plots of a) PPy($Cl^-$), b) PPy/H-ZSM-5-23, c) PPy/H-ZSM-5-80 and d) PPy/H-ZSM-5-280 base ISEs recorded in $10^{-2}$ to $10^{-7}$ M KCl solutions and then back to $10^{-2}$ M KCl solution. The curve marked with A is the calibration plots obtained after conditioning in $10^{-3}$ M KCl solution for 2 days, and the one with B is after conditioning in $10^{-3}$ M KCl for additional 6 days after the 2 days (***Fig. 9, Paper IV***)

The impedance spectra of the PPy($Cl^-$)/ISM and PPy/H-ZSM-5/ISM electrodes were recorded at the open-circuit dc-potential in 0.1 M KCl solution (frequency range = 10 mHz – 100 kHz, $\Delta E_{ac}$ = 5 mV) after the long-term potentiometric test, and the results are compared with the same electrodes when they were freshly prepared. As can be seen in Fig. 28, PPy($Cl^-$)/ISM as well as the PPy/H-ZSM-5/ISM electrodes show a high-frequency semicircle (1.1 – 1.5 MΩ), which is due to the bulk resistance (in parallel with the geometric capacitance) of the PVC-based ion-selective membrane placed on top of the solid contact. After the long-term potentiometric test, the increase of the bulk resistance of PPy($Cl^-$)/ISM, PPy/H-ZSM-5-23/ISM, PPy/H-ZSM-5-80/ISM and PPy/H-ZSM-5-280/ISM is ca 0.20, 0.17, 0.06 and 0.11 MΩ. Such an increase in the bulk resistance upon conditioning is common for plasticized PVC-based ion-selective membranes

and can be related to e.g. water uptake by the membrane. The high-frequency semicircle is followed by a low-frequency tail which can be related to the ion-to-electron transduction process at the solid contact [116]. It is particularly interesting to note that the lowest-frequency impedance (*-Z''*) is lower for all PPy/H-ZSM-5/ISMs compared to the PPy($Cl^-$)/ISM, although the opposite was observed for the bare solid contacts (without ISM) in 0.1 M KCl solution (Fig. 25). This indicates that the redox capacitance of the PPy/zeolite composites can be better utilized than that of PPy($Cl^-$) when they are coated with a plasticized PVC membrane.

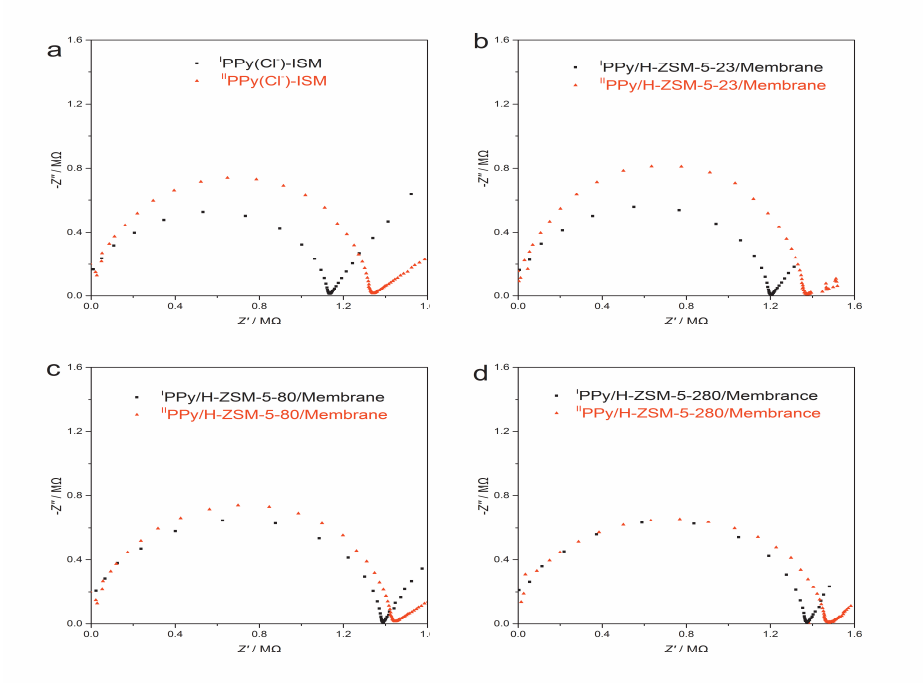


Fig. 28 Impedance spectra of a) PPy($Cl^-$)/ISM, b) PPy/H-ZSM-5-23/ISM, c) PPy/H-ZSM-5-80/ISM and d) PPy/H-ZSM-5-280/ISM. The spectra marked with I were obtained for a freshly prepared electrode and II were obtained after the long-term potentiometric test (ca 8 days). The spectra were recorded at the open-circuit dc-potential in 0.1 M KCl solution, frequency range = 10 mHz − 100 kHz, $\Delta E_{ac}$ = 5 mV (***Fig. 11. Paper IV***)

# 6. CONCLUSIONS

In this thesis, a potentiometric titration method was developed to characterize the anionic groups in the zeolite framework. These anionic groups functioned as the counter ions for PPy in the following chemical and electrochemical synthesis of PPy/zeolite composites. The electrodeposited PPy/zeolite films were tested as a solid contact in $K^+$-ISEs.

Potentiometric titration of zeolites with a strong base in aqueous solutions at room temperature is proved to be a useful method to characterize the anionic groups in microporous and mesoporous materials. The Brønsted and Lewis acid groups can be distinguished based on the data analysis by the Gran method as well as the FITEQL program. The concentrations of the acid groups in the zeolite frameworks, determined by potentiometric titration, are much higher than when determined with the FTIR-pyridine method. The higher concentrations observed are attributed to the small size of the $OH^-$ ions used in the potentiometric titration. These small ions can penetrate deep into the zeolite channels and therefore the acid groups even in those channels can be determined. Although small amounts of aluminum and silicon were found to break away from the studied zeolite during titration, the basic frameworks of the titrated zeolites were still maintained. The Al remains in the titrated zeolites are attributed to the tetrahedral framework $Al^{IV}$.

According to the chemically prepared PPy/H-Beta composites, the decreased surface area and micropore volume of H-Beta zeolites is due to the PPy formed inside the zeolite channels as well as on the surface of the zeolite particles. However, the zeolite framework is maintained in the synthesis reaction. The surface area of the composite can be modified from hundreds of $m^2/g$ to tens of $m^2/g$ by varying the loaded amount of PPy to the zeolite structure. The absorption peaks in the FTIR spectrum of the PPy($Cl^-$) are also observed in the spectrum of the PPy/H-Beta zeolite composites but at slightly lower wavenumbers. The increase in the conductivities of PPy/zeolite compared with PPy($Cl^-$) may be attributed to the enhanced alignment of the polymer chains on the well-ordered zeolite framework. A high $SiO_2/Al_2O_3$ ratio, i.e. low concentration of Brønsted acid groups of the host zeolite, seems to have a negative effect on the electrical conductivity of the polymer/zeolite composite.

During the electrochemical synthesis of PPy/zeolites composites, the anionic groups in the zeolite framework functioned as the counter ions for PPy. All the composites deposited on the Pt electrode exhibited well-defined voltammetric responses for the redox system of $[Ru(NH_3)_6]^{2+}/[Ru(NH_3)_6]^{3+}$, indicating a full coverage of the Pt substrate by the composite. Variations in the cyclic voltammograms of the different composites can be related to the different concentrations of the anionic groups and also the structural properties of the host zeolites. PPy/zeolite composite films had an uneven surface which was composed of PPy and zeolite particles. The thickness of the composite film depended on the concentration of the anionic groups in the host zeolite, i.e. the polymerization of pyrrole propagated more efficiently with the zeolites that contained more anionic groups. PPy was formed on the particle surface and also in the channels of the zeolite, and this process did not influence the zeolite framework.

Although the H-ZSM-5 zeolites are known to be hydrophobic materials, the hydrophobicity of the PPy/H-ZSM-5 composite was determined mainly by PPy. There was no aqueous layer formed between the composite film and the ISM even when the membrane has notoriously high water uptake behavior. All the $K^+$-ISEs using PPy/H-ZSM-5 as SC were sensitive to $K^+$ in the concentration range $10^{-2}$ – $10^{-5}$ M with sub-Nernstian slopes. Compared with the PPy($Cl^-$)-based ISE, the detection limits of the PPy/H-ZSM-5-ISEs were found to be enhanced with an additional 6 days conditioning in $10^{-3}$ M KCl solution. The standard deviation of the $E^0$ value of the composite ISE increased as the acidity of the combined zeolite decreased. Importantly, impedance spectra showed that the redox capacitance of the PPy/zeolite composite was better utilized than that of PPy($Cl^-$) after they were coated with a plasticized PVC membrane.

## REFERENCE


[1] R.M. Latonen, J.E. Lönnqvist, L. Jalander, K. Fröberg, C. Kvarnström, A. Ivaska, Synth Met 156 (2006) 878-884.
[2] R.T. Ahuja, D. Kumar, Sens Actuators B 136 (2009) 275-286.
[3] K.R. Reddy, K.P. Lee, Y. Lee, A.L. Gopalan, Mater Lett 62 (2008) 1815-1818.
[4] W. Chen, C.M. Li, P. Chen, C.Q. Sun, Electrochim Acta 52 (2007) 2845-2849.
[5] C.R. Zhang, Q.L. Li, J.Q. Li, Synth Met 160 (2010) 1699-1703.
[6] X. Li, I. Zhitomirsky, J Power Sources 221 (2013) 49-56.
[7] Y.Q. Han, Y. Lu, Compos Sci Technol 69 (2009) 1231-1237.
[8] A. Mihranyan, L. Nyholm, A.E.G. Bennett, M. Strømme, J Phys Chem 112 (2008) 12249-12255.
[9] D.W. Hatchett, M. Josowicz, Chem Rev 108 (2008) 746-769.
[10] A. Walcarius, Electroanal 20 (2008) 711-738.
[11] O. Kresnawahjuesa, G.H. Kühl, R.J. Gorte, C.A. Quierini, Catal 210 (2002) 106-115.
[12] C. Baerlocher, L.B. McCusker, D.H. Olson, Atlas of Zeolite Framework Types, Elsevier B. V., Amsterdam, 2007.
[13] A. Walcarius, Electroanal 27 (2015) 1303-1340.
[14] J. Weitkamp, Solid State Ionics 131 (2000) 175-188.
[15] I.E. Yuzay, R. Auras, H. Soto-Valdez, S. Selke, Polym Degrad Stabil 95 (2010) 1769-1777.
[16] S. Montalvo, L. Guerrero, R. Borja, E. Sanchez, Z. Milan, I. Cortes, M. Rubia, Appl Clay Sci 58 (2012) 125-133.
[17] P. Mäki-Arvela, B. Holmbom, T. Salmi, D.Y. Muzin, Catal Rev 49 (2007) 197-340.
[18] W.M. Meier, D.H. Olson, Adv Chem Ser 101 (1971) 155-170.
[19] M.G. Valdes, A.I. Perez-Cordoves, M.E. Diaz-Garcia, Trend Anal Chem 25 (2006) 24-30.
[20] L.B. McCusker, C. Baerlocher, in: J. Cejka, H. Van Bekkum, A. Corma and F. Schüth (Eds.), Introduction to zeolite science and practice, ELSEVIER, Amsterdam, 2007, p. 13-38.
[21] A. Dyer, in: J. Cejka, H. van Bekkum, A. Corma and F. Schuth (Eds.), Introduction to zeolite science and practice, 3rd revised edition, Studies in Surface Science and Catalysis , Elsevier B.V., 2007, p. 525-553.
[22] E. Alvarze-Ayuso, A. Garcia-Sanchez, X. Querol, Water Res 37 (2003) 4855-4862.
[23] C.N. Costa, P.G. Savva, A.A. Zorpas, in: V.J. Inglezakis and A.A. Zorpas (Eds.), Handbook of Natural Zeolites, Bentham, 2012, p. 103-132.
[24] A.D. Roberts, X. Li, H.F. Zhang, Chem Soc Rev 43 (2014) 4341-4356.
[25] A. Aho, N. Kumar, K. Eranen, T. Salmi, M. Hupa, D.Y. Murizin, Fuel 87 (2008) 2493-2501.
[26] M. Kangas, N. Kumar, E. Harlin, T. Salmi, D.Y. Murzin, Ind Eng Chem Res 47 (2008) 5402-5412.
[27] B. Silva, H. Figueiredo, O.S.G.P. Soare, M.F.R. Pereira, J.L. Figueiredo, A.E. Lewandowska, J.A. Lercher, M.A. BaNares, I.C. Neves, T. Tavares, Appl Catal B 117-118 (2012) 406-413.
[28] B.L. Bleken, L. Mino, F. Giordanino, P. Beato, S. Svelle, K.P. Lillerud, S. Bordiga, Coordin Chem Rev 15 (2013) 13363-13370.
[29] L.B. McCusker, C. Baerlocher, in: J. Cejka, H. Van Bekkum, A. Corma and F. Schüth (Eds.), Introduction to Zeolite Science and Practice, Elsevier B.V., Amsterdam, 2007.

[30] J.A. Lercher, A. Jentys, in: F. Schüth, K.S.W. Sing and J. Weitkamp (Eds.), Handbook of Porous Solids, Wiley-VCH, Weinheim, 2002, p. 1097.
[31] K.H. Lee, J. Anal. Appl. Pyrolysis 94 (2012) 209-214.
[32] A.K. Aboul-Gheit, A.E. Awadallah, J Nat Gas Chem 18 (2009) 71-77.
[33] S.B. Wang, Y.L. Peng, Chem Eng J 156 (2010) 11-24.
[34] K. Ramesh, D.D. Reddy, Adv Agron 113 (2011) 219-241.
[35] T.Y. Wang, S.H. Yang, K. Sun, X.F. Fang, Ceram Int 37(2) (2011) 621-626.
[36] Y.A. Mustafa, M.J. Zaiter, J Hazard Mater 196 (2011) 228-233.
[37] A. Auroux, Mol Sieves 6 (2008) 45-152.
[38] J.W. Ward, Phys Chem 72 (1968) 4211-4223.
[39] J.W. Ward, Catal 10 (1968) 34-46.
[40] C.M. Naccache, Y.B. Taarit, Catal 22 (1971) 171-181.
[41] T. Baba, Y. Ono, Zeolites 7 (1987) 292-294.
[42] T. Baba, N. Komatsu, H. Sawada, Y. Yamaguchi, T. Takahashi, H. Suglsawa, Y. Ono, Langmuir 15 (1999) 7894-7896.
[43] J.C. Groen, L.A.A. Peffer, J.A. Moulijin, J. Perez-Ramirez, Chem Eur J 11 (2005) 4983-4994.
[44] A.N.C. van Laak, L. Zhang, A.N. Parvulescu, P.C.A. Bruijnincx, B.M. Weckhuysen, K.P. de Jon, P.E. de Jongh, Catal Today 168 (2011) 48-56.
[45] R. Carson, E.N. Cooke, J. Dwter, A. Hinchliffe, P.J. O'Malley, Stud Surf Sci Catal 46 (1989) 39-48.
[46] N. Katada, K. Suzuki, T. Noda, G. Sastre, M. Niwa, J Phys Chem C 113 (2009) 19208-19217.
[47] C.T.W. Chu, C.D. Chang, J Phys Chem 89 (1985) 1569-1571.
[48] N. Batalha, S. Morisset, L. Pinard, I. Maupin, J.L. Lemberton, F. Lemos, Y. Pouilloux, Micropor Mesopor Mat 166 (2013) 101-166.
[49] F. Jin, Y.D. Li, Catal Today 1-2 (2009) 101-107.
[50] L. Rodriguez-Gonzalez, F. Hermes, M. Bertmer, E. Rodriguez-Castellon, A. Jimenez-Lopez, U. Simon, Appl Catal A 328 (2007) 174-182.
[51] M. Käldström, N. Kumar, D.Y. Murzin, Catal Today 167 (2011) 91-93.
[52] M. Käldstöm, N. Kumar, T. Salmi, D.Y. Murzin, Cellul Chem Technol 44 (2010) 203-209.
[53] H.A. Benesi, J Am Chem Soc 78(21) (1956) 5490-5494.
[54] P. Janos, S. Krizenecka, L. Madronova, React Funct Polym 68 (2008) 242-247.
[55] A.E. Hirschler, A. Schneider, J Chem Eng Data 6(2) (1961) 313-318.
[56] A. Streitwieser, Y.J. Kim, J Am Chem Soc 122 (2000) 11783-11786.
[57] E.G. Derouane, J.C. Védrine, R.R. Pinto, P.M. Borges, L. Costa, M.A.N.D.A. Lemos, F. Lemos, R.R. Ribeiro, Cat Rev Sci Eng 55 (2013) 454-515.
[58] A. Jentys, J.A. Lercher, in: H. Van Bekkum, E.M. Flanigen, P.A. Jacobs and J.C. Jansen (Eds.), Studies in Surface Science and Catalysis-Introduction to Zeolite Science and Practice, Elsevier BV, Amsterdam, 2001, p. 345.
[59] P. Sørensen, Kem Maanedsblad 32 (1951) 73.
[60] G. Gran, Analyst 77 (1952) 661-671.
[61] F. Ingman, E. Still, Talanta 13 (1966) 1431-1442.
[62] A. Ivaska, E. Wänninen, Anal Lett 6 (1973) 961-967.
[63] A. Herbelin, J.C. Westall, Department of Chemistry, Oregon State Univeristy 99-01 (1999) .
[64] P.P. Su, (2012) 27.

[65] H. Shirakawa, E.J. Louis, A.G. MacDiarmid, C.K. Chiang, A.J. Heeger, J Chem Soc, Chem Commun 16 (1977) 578-580.
[66] J.L. Brédas, R. Silbey, Conjugated Polymers:The Novel Science and Technology of Highly Conducting and Nonlinear Optically Active Materials, Springer Science + Business Media, B.V., 1991, p. 624.
[67] G. Inzelt, Conducting polymers: A New Era in Electrochemistry, Springer, 2008, p. 123-145.
[68] F. Scholz, Electroanalytical Methods: Guide to Experiments and Applications, Springer, Heidelberg, 2010.
[69] J. Kankare, in: D.L. Wise, G.E. Wnek, T.M. Cooper and J.D. Gresser (Eds.), Electrical and Optical Polymer Systems, Marcel Dekker, Inc. New York, 1998, p. 167-198.
[70] J. Heinze, in: H. Lund and O. Hammerich (Eds.), Organic Electrochemistry, Marcel Dekker, New York, 2001.
[71] P. Audebert, F. Miomandre, in: T.A. Skotheim and J.R. Reynolds (Eds.), CRC Press, 2007, p. 18.
[72] G.G. Wallace, G.M. Spinks, L.A.P. Kane-Maguire, P.R. Teasdale, Conductive Electroactive Polymer, Intelligent Materials and Applications, CRC Press, 2003, p. 51-88.
[73] J. Heinze, B.A. Forntana-Uribe, S. Ludwigs, Chem Rev 110 (2010) 4724-4771.
[74] A.G. MacDiarmid, Synth Met 125(1) (2001) 11-22.
[75] A.J. Heeger, N.S. Sariciftci, E.B. Namdas, Semiconducting and Metallic Polymers, Oxford University Press, 2010, p. 1-17.
[76] R. Kiebooms, R. Menon, K. Lee, in: H.S. Nalwa (Ed.), Advanced Electronic and Photonic Materials and Devices, Academic Press, 2001, p. 1-102.
[77] T.L. Das, S. Prusty, Polym-Plast Technol 51 (2012) 1487-1500.
[78] M. Atesa, T. Karazehir, A.S. Sarac, Curr Phys Chem 2 (2012) 224-240.
[79] E.G. Pineda, F. Alcaide, M.J.R. Presa, A.E. Bolzan, C.A. Gervasi, Appl Mater Interfaces 7 (2015) 2677-2687.
[80] T. Dai, X. Yang, Y. Lu, Mater Lett 61 (2007) 3142-3145.
[81] K.K. Kanazawa, A.F. Diaz, R.H. Geiss, W.D. Gill, J.F. Kwak, J.A. Logan, J.F. Rabolt, G.B. Street, J Chem Soc, Chem Commun 19 (1979) 854-855.
[82] A.F. Diaz, J.I. Castillo, J.A. Logan, W.Y. Lee, J Electroanal Chem 129 (1981) 115-132.
[83] N. Furukawa, K. Nishio, in: B. Scrostai (Ed.), Applications of Electroactive Polymers, Chapman&Hall, London, 1993, p. 150.
[84] G.B. Street, T.C. Clarke, R.H. Geiss, V.Y. Lee, A. Nazzal, P. Pfluger, J.C. Scott, J Phys Colloq C3 (1983) 599-606.
[85] S. Machida, S. Miyata, A. Techagumpuch, Synth Met 31 (1989) 311-318.
[86] S. Rapi, V. Bocchi, G.P. Gardin, Synth Met 24 (1988) 217-221.
[87] T.H. Chao, J. March, J Polym Sci Part A: Polym Chem 26 (1988) 743-753.
[88] R. Ansari, J Chem 3 (2006) 186-201.
[89] S. Sadki, P. Schottland, N. Brodie, G. Sabouraud, Chem Soc Rev 29 (2000) 283-293.
[90] H. Eisazadeh, G. Spinks, G.G. Wallace, Polym 35 (1994) 3801-3803.
[91] M.N. Akieh-Pirkanniemi, (2012) 17-18.
[92] M.M. Gvozdenovic, B.Z. Jugovic, J.S. Stevanovic, B.N. Grgur, Hem Ind 68(6) (2014) 673-684.
[93] R. Greef, R. Peat, L.M. Peter, D. Pletcher, J. Robinson, Instrumental Methods in Electrochemistry, Ellis Horwood Limited, 1993, p. 178-228.

[94] N.S. Sundaresan, in: D.L. Wise, G.E. Wnek, D.J. Trantolo, T.M. Cooper and J.D. Gresser (Eds.), Electrical and Optical Polymer Systems, Marcel Dekker, New York, 1998, p. 97-136.
[95] D. Pletcher, R. Greef, L.M. Peter, J. Robinson, Instrumental Methods in Electrochemistry, Horwood Publishing, Chichester, 2001, p. 178-228.
[96] D.C. Harris, Quantitative Chemical Anlysis, W.H. Freeman and Company, 2010, p. 467-475.
[97] M.W. Urban, Attenuated Total Reflection Spectroscopy of Polymers, American Chemical Society, Washington DC, 1996, p. 3-14.
[98] P.R. Griffiths, J.A. de Haseth, Fourier Transform Infrared Spectrometry 2nd Ed., John Wiley & Sons, Hoboken, 2007, p. 321-348.
[99] M. Claybourn, in: J.M. Chalmers and P.R. Griffiths (Eds.), Handbook of Vibrational Spectroscopy, Theory and Instrumentation, John Wiley & Sons, 2002, p. 969-981.
[100] D. Coster, A.L. Blumenfeld, J. Fripiat, J Phys Chem 98 (1994) 6201-6211.
[101] P.W. Schinler, H.R. Kamber, Helv Chim Acta 51 (1968) 1781-1786.
[102] R.K. Iler, in: Anonymous , The Chemistry of Silica, Johan Wiley and Sons, New York, 1979, p. 180-183 and references there in.
[103] A. Aho, N. Kumar, K. Eränen, T. Salmi, M. Hupa, D.Y. Murzin, Trans IChemE, Part B 85(B5) (2007) 473-480.
[104] A. Aho, N. Kumar, K. Eränen, M. Ziolek, P. Decyk, A.V. Lashkul, T. Salmi, B. Holmbom, M. Hupa, D.Y. Murzin, Fuel 89 (2010) 1992-2000.
[105] V. Bolis, C. Busco, J Phys Chem 110 (2006) 14849-14859.
[106] D.H. Olson, W.O. Haag, W.S. Borghard, Micropor Mesopor Mat 35-36 (2000) 435-446.
[107] R. Hajjar, Y. Millot, P.P. Man, M. Che, S. Dzwigaj, J Phys Chem C 112 (2008) 20167-20175.
[108] D.P.B. Peixoto, S.M. Cabral de Menezes, M.I. Pais da Silva, Mater Lett 57 (2003) 3933-3942.
[109] H.A. Benesi, A.C. Jones, J Phys Chem 63(2) (1959) 179-182.
[110] C.M.B. Gómez, J.M. Juarez, M.L. Martinez, A.R. Beltramone, J. Cussa, O.A. Anunziata, Mater Res Bull 48 (2013) 661-667.
[111] L.H. Xu, F. Yang, C. Su, L.L. Ji, C. Zhang, Electrochim Acta 130 (2014) 148-155.
[112] Y. Furulawa, S. Tazawa, Y. Fujii, I. Harada, Synth Met 24 (1988) 329-341.
[113] E. Lindner, R.E. Gyurcsanyi, J Solid State Electr 13 (2009) 51-68.
[114] M. Fibbioli, W.E. Morf, M. Badertscher, N.F. De Rooij, E. Pretsc, Electroanal 12 (2000) 1286-1292.
[115] R.P. Buck, E. Lindner, Pure Appl Chem 66 (1994) 2527-2536.
[116] J. Bobacka, Anal Chem 71 (1999) 4932-4937.

# SUPPLEMENTARY INFORMATION

**Derivation of a linear potentiometric titration curve**

***Strong acid–strong base***

A strong acid $HR$is completely dissociated:

$$HR \rightarrow H^+ + R^- \qquad \text{(S1)}$$

and the total concentration of the acid $C_{HR}$ is:

$$C_{HR} = [H^+] \qquad \text{(S2)}$$

The titration reaction can be described by the following equation:

$$H^+ + OH^- \rightarrow H_2O \qquad \text{(S3)}$$

The initial volume of the acid is $V_0$, the volume of added base is $V$ and its concentration $C_{OH}$. At each titration point the following mass balance is valid:

$$V_0 C_{HR} = [H^+] \cdot (V_0 + V) + V \cdot C_{OH} \qquad \text{(S4)}$$

If the consumption of the strong base at the equivalence point is denoted by $V_{eq}$ the following equation is valid at the equivalence point:

$$V_0 \cdot C_{HR} = V_{eq} \cdot C_{OH} \qquad \text{(S5)}$$

Combination of equations S4 and S5 gives:

$$V_{eq} - V = \frac{(V_0+V)}{C_{OH}} \cdot [H^+] \qquad \text{(S6)}$$

When $\frac{(V_0+V)}{C_{OH}} \cdot [H^+]$ is plotted as a function of $V$ a straight line is obtained intersecting the $V$-axis at $V_{eq}$. Equation (S6) is valid for the titration points before the equivalence point. With the same analogy, the equation valid for points after the equivalence point can be derived:

$$V - V_{eq} = \frac{(V_0+V)}{C_{OH}} \cdot [OH^-] \qquad \text{(S7)}$$

If the titration data from a potentiometric titration of strong acid with strong base is evaluated two straight lines will be obtained intersecting each other on the $V$-axis at the equivalence point $V_{eq}$.

***Weak acid–strong base***

When a weak acid $HR$ is titrated with a strong base the following reaction takes place:

$$HR + OH^- \rightarrow R^- + H_2O \quad \text{(S8)}$$

The acid takes also part in the following equilibrium:

$$HR \rightleftharpoons H^+ + R^- \quad \text{(S9)}$$

with the protonation constant:

$$K = \frac{[HR]}{[H^+][R^-]} \quad \text{(S10)}$$

The total concentration of the acid, $C_{HR}$, is:

$$C_{HR} = [HR] + [R^-] \quad \text{(S11)}$$

The following mass balance is valid at each titration point:

$$V_0 \cdot C_{HR} = (V_0 + V) \cdot ([HR] + [R^-]) \quad \text{(S12)}$$

and according to reaction (S8) the following equation can be written after each addition of the strong base:

$$V_0 \cdot C_{HR} = (V_0 + V) \cdot [R^-] \quad \text{(S13)}$$

Combination of equations (S10), (S12), (S13) and (S5) gives:

$$V_{eq} - V = K \cdot [H^+] \cdot V \quad \text{(S14)}$$

When the term $[H^+] \cdot V$ is plotted as a function of $V$ a straight line is obtained and it intersects the $V$-axis at $V_{eq}$. The slope of the line is $\frac{1}{K}$. This method allows simultaneous determination of both $V_{eq}$ and $K$. It should be pointed out that equation (S14) is valid so far the acid HR does not take part in any other equilibrium reaction than (S9). When the material, as zeolites in this study, having several acid groups with different strengths is titrated, the entire titration curve when processed with the equation (S14) will consists of linear sections with different slopes, i.e. $K$. When one linear section is converted to the following some curvature will appear on the line. In the evaluation of the titration values for both $V_{eq}$ and $K$, and for each equilibrium only the linear parts should be used.

ISBN 978-952-12-3538-2 (printed edition)
ISBN 978-952-12-3539-9 (digital edition)
Painosalama Oy – Turku, Finland 2017